MORPHOLOGIES OF $\sim 190,000$ GALAXIES AT z=0-10 REVEALED WITH HST LEGACY DATA II. EVOLUTION OF CLUMPY GALAXIES

Takatoshi Shibuya 1, Masami Ouchi $^{1,2},$ Mariko Kubo 1, and Yuichi Harikane 1,3 $Submitted\ to\ ApJ\ November\ 23,\ 2015$

ABSTRACT

We investigate evolution of clumpy galaxies with the Hubble Space Telescope (HST) samples of $\sim 190,000$ photo-z and Lyman break galaxies at $z\simeq 0-8$. We detect clumpy galaxies with off-center clumps in a self-consistent algorithm that is well tested with previous study results, and measure the number fraction of clumpy galaxies at the rest-frame UV, $f_{\rm clumpy}^{\rm UV}$. We identify an evolutionary trend of $f_{\rm clumpy}^{\rm UV}$ over $z\simeq 0-8$ for the first time: $f_{\rm clumpy}^{\rm UV}$ increases from $z\simeq 8$ to $z\simeq 1-3$ and subsequently decreases from $z\simeq 1$ to $z\simeq 0$, which follows the trend of Madau-Lilly plot. A low average Sérsic index of $n\simeq 1$ is found in the underlining components of our clumpy galaxies at $z\simeq 0-2$, indicating that typical clumpy galaxies have disk-like surface brightness profiles. Our $f_{\rm clumpy}^{\rm UV}$ values correlate with physical quantities related to star formation activities for star-forming galaxies at $z\simeq 0-7$. We find that clump colors tend to be red at a small galactocentric distance for massive galaxies with $\log M_*/M_\odot \gtrsim 11$. All of these results are consistent with a picture that a majority of clumps form in the violent disk instability and migrate into the galactic centers.

Subject headings: cosmology: observations — early universe — galaxies: formation — galaxies: high-redshift

1. INTRODUCTION

Galaxy morphology offers invaluable insights into the galaxy formation and evolution. Nearby and low-z galaxies are categorized mainly into three morphological types, i.e., spirals, spheroids, and irregular systems (the Hubble sequence; Hubble 1926). In contrast to this low-z morphological classification, observations with Hubble Space Telescope (HST) have revealed that galaxies with clumpy structures are more abundant at $z\simeq 1-3$ than the local Universe (e.g., Cowie et al. 1995; van den Bergh et al. 1996; Giavalisco et al. 1996; Elmegreen et al. 2004; Elmegreen & Elmegreen 2005, 2006; Elmegreen et al. 2005, 2008, 2009a,b, 2013; Kubo et al. 2013, 2015; Glazebrook 2013; Tadaki et al. 2014; Murata et al. 2014; Guo et al. 2015; Huertas-Company et al. 2015; Garland et al. 2015; Bournaud 2015).

Physical properties of the clumps have been intensively investigated by imaging observations with Advanced Camera for Survey (ACS) and Wide Field Camera 3 (WFC3)/IR-channel on board HST. Spectral energy distribution (SED) analyses with HST multi-wavebands suggest that typical clumps have a stellar mass of $\log M_*/M_{\odot} \simeq 8-9$ and young stellar ages of $\lesssim 0.5$ Gyr (e.g., Guo et al. 2012; Wuyts et al. 2012). Combined with gravitational lensing effects, the high spatial resolving power of HST reveals that the size of clumps ranges from $\simeq 0.1$ kpc to $\simeq 1$ kpc (e.g., Swinbank et al. 2009; Jones et al. 2010; Wisnioski et al. 2012; Livermore et al. 2012, 2015).

Electronic address: shibyatk_at_icrr.u-tokyo.ac.jp

¹ Institute for Cosmic Ray Research, The University of Tokyo,
 5-1-5 Kashiwanoha, Kashiwa, Chiba 277-8582, Japan
 ² Kavli Institute for the Physics and Mathematics of the Uni-

² Kavli Institute for the Physics and Mathematics of the Universe (Kavli IPMU, WPI), University of Tokyo, Kashiwa, Chiba 277-8583, Japan

³ Department of Physics, Graduate School of Science, The University of Tokyo, 7-3-1 Hongo, Bunkyo, Tokyo, 113-0033, Japan

Even in substantial observational efforts, the clump formation mechanisms have not been fully understood. Two viable candidates have been proposed as a clump formation mechanism: 1) the violent disc instability (VDI; e.g., Noguchi 1998) and 2) galaxy mergers (e.g., Di Matteo et al. 2008, although cf. Taniguchi & Shioya 2001). The former and the latter are the "in-situ" and "ex-situ" origins for clumps, respectively. In the case of VDI, clumps are predicted to form in unstable regions where the Toomre Q parameter (Toomre 1964) is below a critical value (an order of unity) in thick and gas-rich galaxy disks (e.g., Immeli et al. 2004a,b; Bournaud et al. 2007, 2009; Dekel et al. 2009a; Ceverino et al. 2010; Tacconi et al. 2010; Agertz et al. 2009, 2015; Forbes et al. 2012). On the other hand, mergers of compact galaxies would also add clumpy components on galaxies, providing the similar clumpy morphology.

The fate of clumps have also been a matter of debate. Theoretical studies and numerical simulations have predicted that clumps at disk regions migrate into the galactic centers due to dynamical frictions and/or clumpclump interactions (e.g., Immeli et al. 2004a,b; Dekel et al. 2009a; Inoue & Saitoh 2012; Ceverino et al. 2012; Mandelker et al. 2014; Inoue et al. 2015). The migrating clumps would subsequently contribute the formation of a central proto-bulge. In contrast, several numerical simulations have suggested that clumps are destroyed by their own and/or galactic feedback before the clump migration (e.g., Genel et al. 2012; Hopkins et al. 2012; Moody et al. 2014). The disrupted clumps could become components of galaxy disks (e.g. Bournaud et al. 2014). These predictions indicate that clumps are important structures for characterizing the morphological evolution of galaxies.

A powerful observational technique is to construct spatial Q and velocity (v) maps on clumpy galaxies for distinguishing the two clump formation mechanisms. Dur-

ing the last decade, three-dimensional kinematic properties for clumpy galaxies have been examined by exploiting adaptive optics systems and integral field spectrographs (IFS) (e.g., Förster Schreiber et al. 2011; Newman et al. 2012; Genzel et al. 2011, 2014). According to these IFS studies, Q values on clump regions tend to be below unity. The low Q value is evidence that clumps have the in-situ origin and form through VDI. The velocity structure also provides important hints of whether clumps are dynamically bounded in host galaxies. The velocity of typical clumps follows global motions of host galaxy disks within $\Delta v \lesssim 200~{\rm km~s^{-1}}$, which suggests the in-situ clump origin (e.g., Bournaud et al. 2008; Wisnioski et al. 2011, 2012, 2013; Sobral et al. 2013; Tacchella et al. 2015; Burkert et al. 2015). In contrast, statistical studies with IFS indicate that ex-situ clumps appear to be rare among $z \simeq 2$ star-forming galaxies (e.g., Shapiro et al. 2008; Bournaud 2015). In the case of the ex-situ origin (i.e. mergers), clumps could show a large velocity offset ($\Delta v \gtrsim 300 \text{ km s}^{-1}$) with respect to host galaxies (e.g. Menéndez-Delmestre et al. 2013).

These results support the picture that a majority of clumps have the in-situ origin for $z \simeq 2$ massive galaxies. As a next step, we examine the major mechanism of clump formation over cosmic time. However, these kinematic analyses are expensive due to requirements of deep IFS spectroscopic observations. Recently, Guo et al. (2015) suggest that an abundance of clumpy galaxies is one of useful probes for investigating clump formation mechanisms. Using HST imaging data, Guo et al. (2015) have systematically measured number fractions of clumpy galaxies in overall galaxy samples (the clumpy fraction; f_{clumpy}) at $z \simeq 0-3$. Comparisons between $f_{\rm clumpy}$ and theoretical predictions suggest that clumps are likely to form in VDI and galaxy mergers for galaxies with $\log M_*/M_{\odot} \gtrsim 11$ and $\lesssim 10$, respectively. However, $f_{\rm clumpy}$ has not still been unveiled beyond $z \simeq 3$. Systematic f_{clumpy} measurements over a wide redshift range would provide useful hints for understanding the major clump formation mechanism and properties of clumpy host galaxies.

In this paper, we investigate the redshift evolution of clumpy galaxies using HST legacy data. We identify clumpy galaxies at $z \simeq 0-8$ in a self-consistent clump detection argorithm using the large galaxy sample. This is the second paper in the series studying the galaxy morphology with the HST samples. 4 The organization of this paper is as follows. In Section 2, we describe the details of the HST galaxy samples. Section 3 shows the HSTimages and galaxies used for our clumpy structure analvses. We present methods to identify clumpy structures in Section 4. In Section 5, we perform Monte Carlo simulations to evaluate the intrinsic clump luminosity and clump detection completeness. We show the redshift evolution of f_{clumpy} , radial surface brightness (SB) profiles of clumpy galaxies, relations between clumps and physical quantities of host galaxies, and clump colors in Section 6. In Section 7, we discuss the implications for clump formation mechanisms. We summarize our findings in

Throughout this paper, we adopt the concordance

cosmology with $(\Omega_m, \Omega_{\Lambda}, h) = (0.3, 0.7, 0.7)$, (Komatsu et al. 2011). All magnitudes are given in the AB system (Oke & Gunn 1983). We refer to the HST F606W, F775W, F814W, F850LP, F098M, F105W, F125W, F140W, and F160W filters as $V_{606}, i_{775}, I_{814}, z_{850}, Y_{098}, Y_{105}, J_{125}, JH_{140}$, and H_{160} , respectively.

2. DATA AND SAMPLES

We use the following two galaxy samples in this study. These galaxy samples are constructed from the deep optical and near-infrared imaging data taken by HST deep extra-galactic legacy surveys. Paper I summarizes the limiting magnitudes and point spread function (PSF) sizes of the HST images.

2.1. Sample of Photo-z Galaxies in 3D-HST+CANDELS

The first sample is made of HST/WFC3-IR detected galaxies with photometric redshifts (hereafter photo-z galaxies) at z = 0 - 6 taken from Skelton et al. (2014). These galaxies are identified in five Cosmic Assembly Near-infrared Deep Extragalactic Legacy Survey (CAN-DELS) fields (Grogin et al. 2011; Koekemoer et al. 2011), and detected in stacked images of J_{125} , JH_{140} , and H_{160} bands of WFC3/IR. The imaging of these IR-bands yields roughly a stellar mass-limited sample. The photometric properties and the results of SED fitting for all the sources are summarized in Skelton et al. (2014). The HST images and catalogues are publicly released at the 3D-HST website. ⁵ We use galaxies whose physical quantities and photometric redshifts are well derived from SED fitting (specifically, sources with use_phot= 1 in the public catalogues). In this paper, we assume Salpeter (1955) initial mass function (IMF). To obtain the Salpeter IMF values of stellar masses (M_*) and star formation rates (SFRs), we multiply the Chabrier (2003) IMF values from the Skelton et al. (2014) catalogue by a factor of 1.8. We divide the sample of photo-z galaxies into two subsamples of star-forming galaxies (SFGs) and quiescent galaxies (QGs) by specific SFR (sSFR) values. Galaxies with sSFR ≥ 0.1 and < 0.1 Gyr⁻¹ are classified as SFGs and QGs, respectively.

Structural parameters such as semi-major axes $(R_{\rm e,major})$, position angle (P.A.), axial ratios (q), circularized effective radii $(r_{\rm e})$, and Sérsic indices (n) have been obtained from our Sérsic profile fitting (Sérsic 1963, 1968) with GALFIT (Peng et al. 2002, 2010). In the GALFIT fitting, clumpy subcomponents of galaxies are masked to acquire these structural parameters of major stellar components. The SFR surface density (SFR SD), $\Sigma_{\rm SFR}$, has been calculated by an equation of $\Sigma_{\rm SFR} = {\rm SFR}/(2\pi r_{\rm e}^2)$. See Paper I for details.

2.2. Sample of LBGs in CANDELS, HUDF09/12, and HFF

The second sample consists of LBGs at $z\simeq 4-10$ made by Y. Harikane et al. (in preparation) in the CANDELS, the *Hubble* Ultra Deep Field 09+12 (HUDF 09+12; Beckwith et al. 2006; Bouwens et al. 2011; Illingworth et al. 2013; Ellis et al. 2013) fields, 6 and the

 $^{^4}$ The first paper presents a study on galaxy sizes at $z\simeq 0-10$ (Shibuya et al. 2015, hereafter Paper I).

⁵ http://3dhst.research.yale.edu/Home.html

⁶ http://archive.stsci.edu/prepds/xdf/

Population			N .(N.)			$N_{ m gal}^{ m total}(N_{ m clumpy}^{ m total})$
1 opulation	$z = 0 - 1^{a}$	$N_{\rm gal}(N_{\rm clumpy})$ $z = 0 - 1^{\rm a}$ $z = 1 - 2$ $z = 2 - 3$ $z = 3 - 4$ $z = 4 - 5$ $z = 5 - 6$					
(1)	$z = 0 - 1^{-1}$ (2)	$z = 1 - 2 \tag{3}$	$z = 2 - 3 \tag{4}$	$z = 3 - 4 \tag{5}$	$z = 4 - 3 \tag{6}$	z = 5 - 6 (7)	(8)
(Photo-z galaxies)							
SFGs (UV)	2187 (859)	3236 (1842)	$14\dot{2}9$ (672)	94 (44)	12 (6)	4(2)	6962 (3425)
QGs (ÙV)	1079 (195)	786 (346)	144 (50)	11 (3)	1 (1)	0 (0)	2021 (595)
SFGs (Opt)	1353 (645)	1624 (534)					2977 (1179)
QGs (Opt)	579 (Ì37)	523 (95)					1102 (232)
	$z \simeq 4$	$z \simeq 5$	$z \simeq 6$	$z \simeq 7$	$z \simeq 8$	$(z \simeq 10^{\rm b})$	
LBGs (UV)	2296 (391)	1150 (158)	277 (32)	106 (11)	19 (3)	0 (0)	3848 (595)

TABLE 1
Numbers of Our Sample Galaxies for Clumpy Structure Analyses and Clumpy Galaxies

Note. — Columns: (1) Galaxy population. The rest-frame wavelength for clumpy structure analyses is given in parentheses. (2)-(7) Numbers of SFGs, QGs and LBGs used for our clumpy structure analyses in each redshift bin. The values in parentheses indicate the numbers of clumpy galaxies in each redshift bin. (8) Total numbers of sample galaxies. The values in parentheses indicate the total numbers of clumpy galaxies.

parallel fields of Abell 2744 and MACS0416 in the Hubble Frontier Fields (e.g., Coe et al. 2014; Atek et al. 2015; Oesch et al. 2014; Ishigaki et al. 2014). These LBGs are selected with the color criteria, similar to those of Bouwens et al. (2014b). We perform source detections by SEXTRACTOR (Bertin & Arnouts 1996) in coadded images constructed from bands of $Y_{098}Y_{105}J_{125}H_{160}$, $J_{125}H_{160}$, and H_{160} for the $z \simeq 4 - 7$, 8, and 10 LBGs, respectively. The JH_{140} band is included in the coadded image for the $z \simeq 7-8$ LBGs in the HUDF09+12 field. The flux measurements are carried out in Kron (1980)type apertures with a Kron parameter of 1.6 whose diameter is determined in the H_{160} band. In two-color diagrams, we select objects with a Lyman break, no extreme-red stellar continuum, and no detection in passbands bluer than the spectral drop. See Y. Harikane et al. (in preparation) for more details of the source detections and LBG selections.

Similarly for the photo-z galaxies, we have obtained $R_{\rm e,major}$, q, and $r_{\rm e}$ for the LBG sample. We note that the LBGs have no Sérsic index measurements due to fixing n values in the GALFIT fitting. We have also derived $\Sigma_{\rm SFR}$ and UV slope β for the LBGs (see Paper I).

3. HST-BAND IMAGES AND GALAXIES FOR CLUMPY STRUCTURE ANALYSES

In this section, we describe HST-band images and galaxies used for our clumpy structure analyses.

3.1. HST-band images

To minimize the effect of morphological K-correction, we use images of HST multi-wavebands. In this study, we investigate clumps at the rest-frame UV $(1500-3000\,\text{Å})$ and optical $(4500-8000\,\text{Å})$ wavelengths. These clumps are hereafter referred to as "UV clumps" and "optical clumps", respectively. For UV clumps, we use V_{606} for z=0-2, I_{814} for z=2-3 photo-z galaxies, and coadded images of $Y_{098}Y_{105}J_{125}H_{160}$ and $J_{125}H_{160}$ for $z\gtrsim 4$ LBGs. For optical clumps, we choose J_{125} for z=0-1 and H_{160} for z=1-2 photo-z galaxies. 7

Guo et al. (2015) have analyzed a larger number of ACS bands, $B_{435}V_{606}i_{775}z_{850}$, for UV clumps in the GOODS-S field compared to ours. Here we restrict our bands to V_{606} and I_{814} for a homogeneous analysis in all the CANDELS fields due to the lack of B_{435} , i_{775} and/or z_{850} in AEGIS, COSMOS and UDS. The difference of these HST band choices has provided no significant impacts on results of clumpy structure analyses (Guo et al. 2015).

3.2. Sample galaxies

We select bright, large, and face-on galaxies from the two galaxy samples (Section 2) for secure identifications of clumpy structures. We analyze photo-z galaxies with $\log M_*/M_{\odot} \geq 9$, $H_{160} < 24.5$ mag, an H_{160} -band semimajor axis of $R_{\rm e,major} \geq 0.22$, and $q \geq 0.5$ in the ACS band images. These selection criteria are the same as those of Guo et al. (2015). We restrict analyses to galaxies with $R_{\rm e,major} \geq 0.44$ for the WFC3/IR band images due to a broader PSF size than that of ACS. In total, 6962 (2977) SFGs and 2021 (1102) QGs are selected for analyses of UV (optical) clumps.

For the LBGs, we apply only a magnitude cut of $m_{\rm UV} < 27$ mag to improve statistics at $z \gtrsim 6$. The total number of LBGs at $z \simeq 4-8$ is 3848 for the clumpy structure analyses. Here we exclude the LBGs at $z \simeq 10$ due to the small statistics. ⁸ The effect of the selection criterion choices is discussed in Sections 6.1.4 and 6.1.5.

Table 1 summarizes the number of photo-z galaxies and LBGs used for our clumpy structure analyses.

4. ANALYSIS

We describe methods to identify clumpy structures in the *HST* images. The clumpy structures of galaxies have been examined in several ways, e.g., by using SEXTRACTOR (e.g., Murata et al. 2014), CLUMPFIND (Williams et al. 1994), the non-parametric morphological indices (e.g., Conselice 2003), and based on the visual inspection (e.g., Elmegreen et al. 2007). Recently, Guo et al. (2015) have developed a well-sophisticated technique to identify

 $^{^{\}rm a}$ The redshift range is confined to z=0.5-1 because of the small galaxy number at $z\lesssim0.5.$

^b The LBGs at $z \simeq 10$ are excluded in our clumpy structure analyses due to the small statistics.

 $^{^7}$ We make use of z_{850} for GOODS-North that has not been observed with the I_{814} band.

⁸ Our visual inspections confirm that the LBGs at $z \simeq 10$ show no clumpy structures (see also, Holwerda et al. 2015).

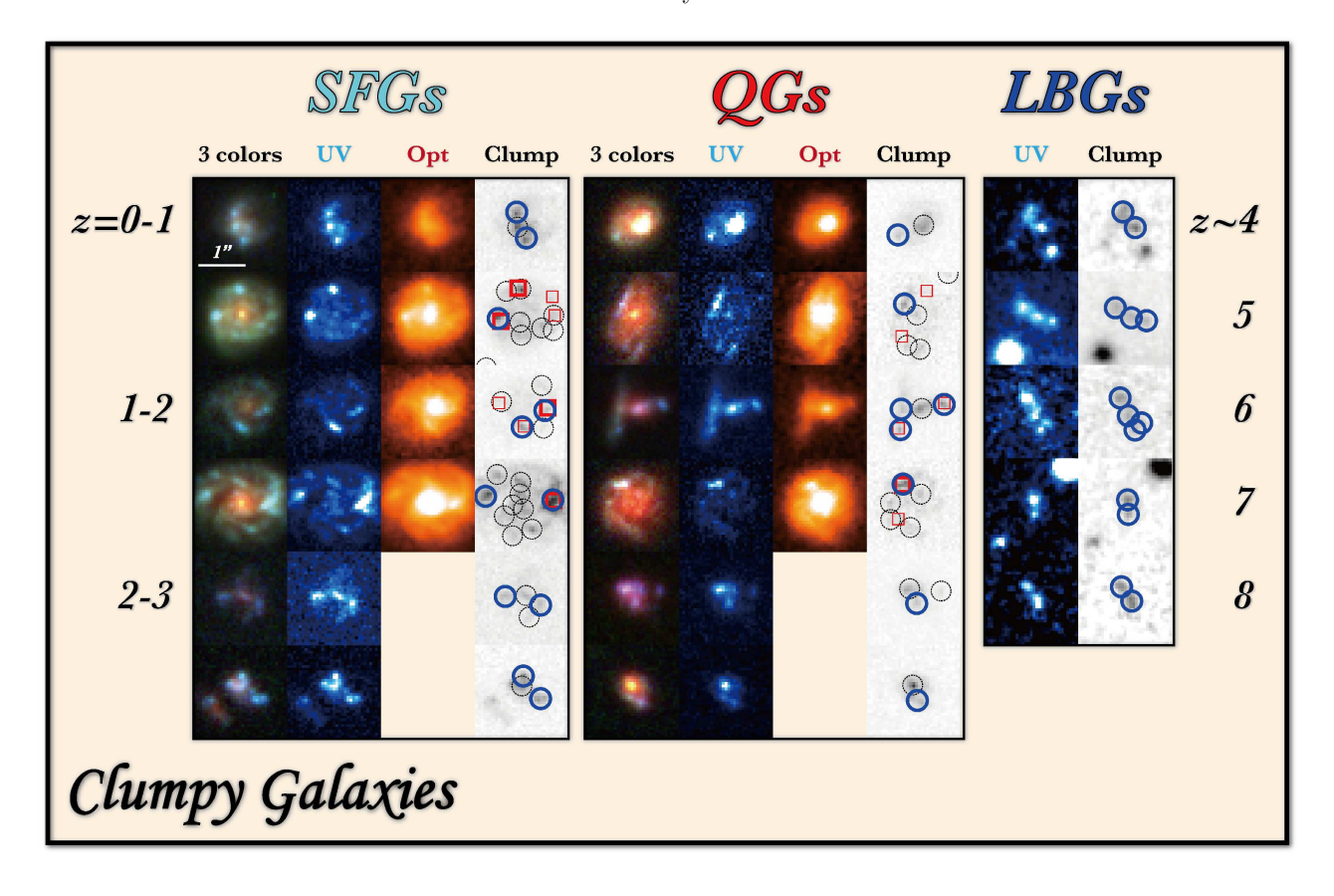


Fig. 1.— Examples of clumpy galaxies identified in our selections. The left, middle, and right panel-sets indicate SFGs, QGs, and LBGs, respectively. Each of the four-panel sets for the SFGs and the QGs presents the three-color composite, the rest-frame UV, the rest-frame optical images, and the clump position maps, from left to right. In the clump position maps, the black and blue circles denote UV clump candidates and selected UV clumps with $L_{\rm cl}/L_{\rm gal} \geqslant 0.08$, respectively. The thick and thin red squares indicate optical clumps with $L_{\rm cl}/L_{\rm gal} \geqslant 0.1$ and $L_{\rm cl}/L_{\rm gal} = 0.08-0.1$, respectively. Each row, from top to bottom, represents example clumpy galaxies from $z \simeq 0$ to $z \simeq 3$. Each of the two-panel sets for the LBGs exhibits the coadded images (left) and the clump position maps (right). Each row, from top to bottom, denotes clumpy LBGs from $z \simeq 4$ to $z \simeq 8$. The white tick indicates the size of 1".

off-center UV clumps in high-z galaxies with ACS images. In this study, we employ a method similar to that of Guo et al. (2015). We also newly apply this technique to both ACS and WFC3/IR images. The identification parameters for the WFC3/IR images are determined by our careful visual inspections.

- 1. Object images we extract $18'' \times 18''$ cutout images from the HST data at the position of each photo-z galaxy and LBG. The size of cutout images is sufficiently large to investigate entire galaxy structures even for extended objects at $z \simeq 0-1$.
- 2. Segmentation maps we also cutout SEXTRACTOR segmentation maps with the same size as for the object images to define areas searching for clumps. We use H_{160} segmentation maps that are generated by our SEXTRACTOR detections and publicly released in the 3D-HST website. SEXTRACTOR frequently outputs segmentation areas smaller than intrinsic galaxy sizes for faint sources. We enlarge individual segmentation areas (so-called "dilation"; see, Guo et al. 2013; Galametz et al. 2013) with a task of GAUSS in IRAF according to isophotal areas of each galaxy. Our dilation technique is slightly different from

- e.g. Galametz et al. (2013) with the TFIT software. We find that the difference of dilated areas provides negligible impacts on our results of our clumpy structure analyses.
- 3. Detection of clumps we detect clumpy objects within galaxies. We first smooth the object images through a boxcar filter with a side of ten pixel (= 0.6). Next, we subtract the smoothed images from the original ones to stand out clumpy objects. These subtracted images are referred to contrast images. To avoid detections of sky noise, we mask all pixels with a flux less than 2σ of sky background fluctuation. Sky background levels are measured in the contrast images after a 3σ flux clipping. Finally, we perform SEXTRACTOR detections within regions defined with the dilated segmentation maps. We require these clumpy objects to have an area larger than five (seven) contiguous pixels, DETECT_MINAREA = 5 (7), for the ACS (WFC3/IR) images. We define "clump candidates" as these detected objects.
- 4. Photometry of clumps we carry out photometry for the clump candidates. We measure an aperture flux, f_{aper} , within a radius of $r_{\text{aper}} = 3$ (6) pixels,

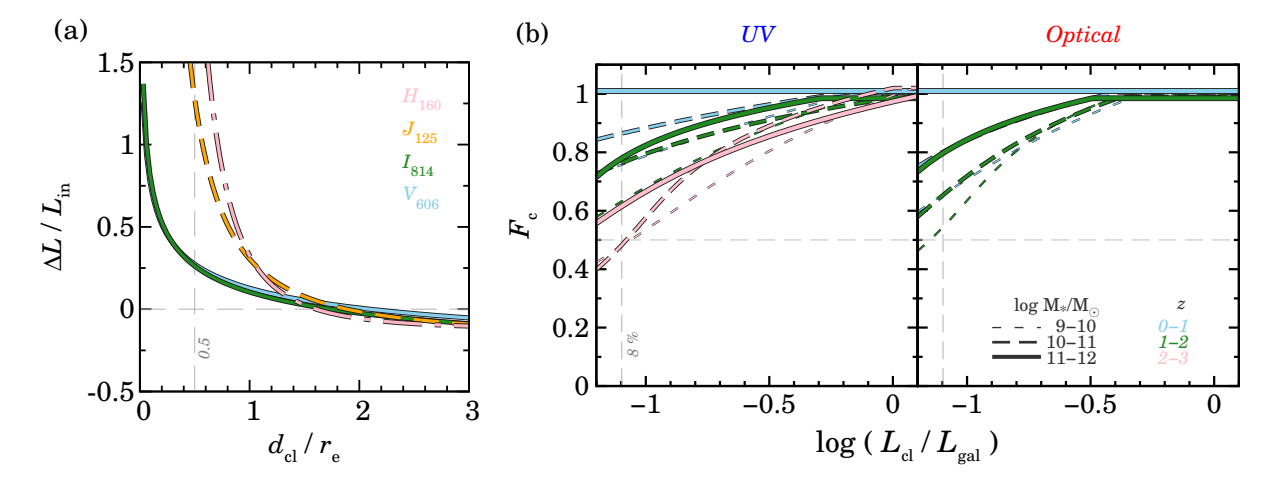


FIG. 2.— Results of the Monte-Carlo simulations for the clump identifications. (a) Luminosity overestimate ratios, $\Delta L/L_{\rm in}$, as a function of $d_{\rm cl}/r_{\rm e}$. The cyan solid, green solid, orange dashed, and magenta dot-dashed curves show $\Delta L/L_{\rm in}$ for the V_{606} , I_{814} , J_{125} , and H_{160} -band images, respectively. The vertical dashed line denotes the inner $d_{\rm cl}/r_{\rm e}$ threshold ($d_{\rm cl}/r_{\rm e}=0.5$; see Section 4 for details). The horizontal dashed line presents $\Delta L/L_{\rm in}=0$. (b) Detection completeness of clumps, F_c , as a function of $L_{\rm cl}/L_{\rm gal}$. The left and right panels indicate F_c in the rest-frame UV and optical wavelengths, respectively. The cyan, green, and magenta curves denote F_c at z=0-1, 1-2, and 2-3, respectively. The short-dashed, long-dashed, and solid curves present $\log M_*/M_{\odot}=9-10$, 10-11, and 11-12, respectively. The horizontal dashed lines denote $F_c=0.5$. The vertical dashed lines indicate the threshold of fractional luminosity, $L_{\rm cl}/L_{\rm gal}=8\%$, for the clump identifications.

corresponding to 0".18 (0".36), for clump candidates in the ACS (WFC3/IR) images. These photometric apertures would include background fluxes of host galaxies. We subtract the background fluxes of host galaxies from $f_{\rm aper}$. The average SB in a circular ring with at r=4-10~(8-20) pixels is considered to be the background fluxes for clump candidates in the ACS (WFC3/IR) images. The background-subtracted $f_{\rm aper}$ is converted to a total flux, $f_{\rm tot}$, by applying aperture corrections. The factors of aperture corrections range from $\simeq 0.7$ to $\simeq 0.8$. We convert $f_{\rm tot}$ to a luminosity, $L_{\rm cl}$, under the assumption that these clump candidates are physically associated with host galaxies.

Guo et al. (2015) find that $L_{\rm cl}$ at a small galactocentric distance, $d_{\rm cl}$, tends to be overestimated due to bright central structures (e.g. bulges). We evaluate these "luminosity overestimate ratios" in Monte-Carlo simulations (Section 5), and correct for $L_{\rm cl}$.

5. Selection of clumps — we select off-center clumps among the clump candidates based on their luminosity and position. We employ the following criteria:

$$L_{\rm cl}/L_{\rm gal} \geqslant 0.08 \&\&$$
 $0.5 \leqslant d_{\rm cl}/r_{\rm e} < 8$ (1)

where $L_{\rm gal}$ is a luminosity of a host galaxy. To measure $d_{\rm cl}$, we use flux-weighted centers determined by the SEXTRACTOR detections of Skelton et al. (2014) and Y. Harikane et al. in preparation. The segmentation areas are typically more effective than the outer boundary of $d_{\rm cl}/r_{\rm e}=8$. In this study, we define "clumpy galaxies" as objects with at least one off-center clump that meets Equation 1.

For the LBG sample, we do not use the $d_{\rm cl}/r_{\rm e}$ criterion. This is because high-z LBGs are unlikely to have an evolved bright cores at the centers. We define clumpy galaxies as objects with at least two clumps that meet only the $L_{\rm cl}/L_{\rm gal}$ criterion in Equation 1.

Figure 1 shows examples of clumpy galaxies. The results of clump identification appears to be in good agreement with visual inspections.

5. LUMINOSITY OVERESTIMATE RATIOS AND DETECTION COMPLETENESS

We perform Monte-Carlo simulations to evaluate luminosity overestimate ratios $(\Delta L/L_{\rm in})$ and detection completeness (F_c) in the same manner as in Guo et al. (2015). First, we create an artificial clump by using MKOB-JECTS in the IRAF package. Second, the artificial clump is broadened to the PSF size of an HST image. Third, the artificial clump is added to a segmentation area of a real galaxy. Here we randomly change luminosity $L_{\rm cl}/L_{\rm gal}$ and position $d_{\rm cl}/r_{\rm e}$ of the artificial clump in ranges of $-2.5 \leqslant \log{(L_{\rm cl}/L_{\rm gal})} < 0$ and $0.1 \leqslant d_{\rm cl}/r_{\rm e} < 3$, respectively. Finally, we detect the artificial clump and carry out photometry in the same manner as for the real galaxies (Section 4). This procedure is repeated 50 times for each galaxy at a given $L_{\rm cl}/L_{\rm gal}$ and $d_{\rm cl}/r_{\rm e}$. We perform the simulation for 1,000 galaxies in each HST band and field.

The panel (a) of Figure 2 shows the luminosity overestimate ratios, $\Delta L/L_{\rm in} \equiv (L_{\rm out}-L_{\rm in})/L_{\rm in}$, as a function of $d_{\rm cl}/r_{\rm e}$, where $L_{\rm in}$ $(L_{\rm out})$ is the input (output) clump luminosity in the Monte-Carlo simulation. As shown in the panel (a), $\Delta L/L_{\rm in}$ gradually increases towards the galactic centers, and reach to $\Delta L/L_{\rm in} \simeq 0.3$ at $d_{\rm cl}/r_{\rm e}=0.5$ for the $V_{606}I_{814}$ images. These trends are consistent with that of Guo et al. (2015). In contrast, we find that the $J_{125}H_{160}$ images have a relatively high value of $\Delta L/L_{\rm in} \simeq 1.5$ at $d_{\rm cl}/r_{\rm e}=0.5$. These high

Reference	Sample $(N_{\rm gal})$	$\log M_*, L_{\mathrm{UV}}$	Redshift	Method	Detection Band
		$(M_{\odot}, L_{z=3}^*)$			
(1)	(2)	(3)	(4)	(5)	(6)
Elmegreen et al. (2007)	Starbursts (1003)	N/A	0 - 5	Visual	i_{775}
Puech (2010)	Emission-line galaxies (63)	$\log M_{*}$ > 10.3	$\simeq 0.6$	Visual	B_{435}
Overzier et al. (2010)	LBAs (30)	$\log M_* = 9 - 11$	$0.1 \sim 0.3$	Visual	UV
Guo et al. (2012)	Star-forming galaxies (10)	$\log M_* > 10$	1.5 - 2.5	Algorithm	z_{850}
Wuyts et al. (2012)	Star-forming galaxies (649)	$\log M_* > 10$	0.5 - 2.5	Algorithm	UV, opt
Taďaki et al. (2014)	HAEs (100)	$\log M_*9 - 11.5$	2 - 2.5	CLUMPFIND	V_{606}, H_{160}
Murata et al. (2014)	$I_{814} < 22.5 \text{ galaxies } (24027)$	$\log M_* > 9.5$	0.2 - 1	Algorithm	I_{814}
Guo et al. (2015)	Star-forming galaxies (3229)	$\log M_* \simeq 9 - 11.5$	$0 \sim 3$	Algorithm	UV
Lotz et al. (2006)	LBGs (82)	$L_{\rm UV} \gtrsim 0.4$	4	$CAGM_{20}$	UV
Ravindranath et al. (2006)	LBGs (1333)	$L_{\mathrm{UV}} \gtrsim 0.7$	3 - 5	Sérsic	UV
Conselice & Arnold (2009)	LBGs (133)	$L_{\mathrm{UV}} \gtrsim 0.3$	$4 - 6^{a}$	$CASGM_{20}$	UV
Oesch et al. (2010)	LBGs (21)	$L_{\rm UV} \gtrsim 0.06$	7 - 8	Visual	UV
Law et al. (2012a)	LBGs (309)	$L_{\rm UV} \simeq 0.3 - 1^{\rm b}$	1.5 - 3.6	$CAGM_{20}$	UV
Jiang et al. (2013) ^c	LBGs (24)	$L_{\rm UV} \gtrsim 0.7$	5.7 - 7	Visual	UV
Kawamata et al. (2014)	LBGs (39)	$L_{\rm UV} \gtrsim 0.04$	6 - 8	Visual	UV
Curtis-Lake et al. (2014)	LBGs (1318)	$L_{\rm UV} \gtrsim 0.3$	4 - 8	A	UV
This work	Photo- z galaxies (13062 ^d)	$\log M_* \simeq 9 - 12$	$0 \sim 6$	G15	UV, opt
	LBGs (3848)	$L_{\mathrm{UV}} \gtrsim 0.3$	$4 \sim 8$	G15	ÚV
	$(N_{\rm gal}^{\rm total} = 16910)$		$0 \sim 8$	G15	UV, opt

NOTE. — Columns: (1) Reference. (2) Galaxy population. The values in parentheses present the numbers of sample galaxies. (3) Stellar mass or UV luminosity ranges. (4) Redshift ranges. (5) Methods to identify clumpy structures ("Visual": visual inspection; "Algorithm": original algorithm in the literature; "CLUMPFIND": the CLUMPFIND software; "C": Concentration; "A": Asymmetry; "S": Clumpiness; "G": Gini coefficient; " M_{20} ": the second-order moment parameter; "Sérsic": Sérsic fitting; "G15": the method of Guo et al. (2015)). See Conselice et al. (2014) for the definition of the non-parametric indices. For comparison in Figure 4, we choose $f_{\rm clumpy}^{\rm UV}$ measured with non-parametric indices (e.g., GM_{20} and A) if the literature has several methods to identify clumps. This is because the non-parametric indices would select clumpy galaxies similar to ours compared to the other methods. (6) Detection bands for clump identifications.

 $\Delta L/L_{\rm in}$ values would result from the broad PSF sizes of $J_{125}H_{160}$ and/or a flux contribution of bright central bulge-like objects at the rest-frame optical wavelengths.

The panel (b) of Figure 2 represents F_c as a function of $L_{\rm cl}/L_{\rm gal}$. We find that clumps are well identified even for low- M_* and high-z galaxies (i.e. $F_c \gtrsim 0.5$ at $L_{\rm cl}/L_{\rm gal} \geqslant 0.08$). We correct for the detection incompleteness by using the following equation,

$$f_{\text{clumpy}}^{\text{cor}} = f_{\text{clumpy}} + \frac{1}{n_c} \left(\frac{1}{F_c} - 1 \right) f_{\text{clumpy}}$$
$$- \frac{1}{n_c} \left(\frac{1}{F_c} - 1 \right) (f_{\text{clumpy}})^2, \tag{2}$$

where $f_{\rm clumpy}^{\rm cor}$ and n_c are an incompleteness-corrected clumpy fraction and the number of clumps in a host galaxy, respectively. We assume $n_c=2$ for incompleteness correction similarly in Guo et al. (2015). The correction with Equation 2 typically makes $f_{\rm clumpy}$ to increase by a factor of $\simeq 1.1-1.2$. We find that F_c is most sensitive to M_* ($\simeq L_{\rm gal}$) and z of host galaxies. For this reason, we correct for the detection incompleteness for the redshift evolution of $f_{\rm clumpy}$ (Section 6.1), but for analyses in a given M_* , $L_{\rm gal}$ and z bin (e.g., Section 6.3.1).

6. RESULTS

6.1. Evolution of Clumpy Fractions

We present our $f_{\rm clumpy}$ measurements for the photo-z galaxies and the LBGs in Section 6.1.1. We compare our $f_{\rm clumpy}$ values for the photo-z galaxies and the LBGs with results of previous studies in Sections 6.1.2 and 6.1.3, respectively. In Section 6.1.4, we show the redshift evolution of $f_{\rm clumpy}$ at $z \simeq 0-8$ in a compilation of the photo-z galaxy and LBG samples. In Section 6.1.5, we check whether our results of $f_{\rm clumpy}$ at $z \simeq 0-8$ are reliable.

6.1.1. Clumpy Fractions for the Photo-z Galaxies and the LBGs

We present f_{clumpy} for the photo-z galaxies at $z \simeq 0-3$ and the LBGs at $z \gtrsim 4$. Figure 3 shows F_c -corrected clumpy fractions $f_{\text{clumpy}}^{\text{cor}}$ for the SFGs and the QGs. We measure the number fraction of galaxies with UV clumps, $f_{\text{clumpy}}^{\text{UV},\text{cor}}$, and optical ones, $f_{\text{clumpy}}^{\text{opt,cor}}$. In Figure 3, galaxies at $z \geqslant 3$ are not shown due to the small statistics (see Table 1).

For the SFGs, we find that $f_{\rm clumpy}^{\rm UV,cor}$ basically decreases from $z \simeq 3$ to $z \simeq 0$ in all the M_* bins. These $f_{\rm clumpy}^{\rm UV,cor}$ evolutions appear to slightly depend on M_* in the sense that $f_{\rm clumpy}^{\rm UV,cor}$ in a high- M_* bin drops quickly towards low-z. In a high- M_* bin of $\log M_*/M_\odot = 11-12$, $f_{\rm clumpy}^{\rm UV,cor}$ has $\simeq 70\%$ at $z \gtrsim 2$, and gradually decreases to $\simeq 20\%$ at $z \simeq 0$. In an intermediate- M_* bin of $\log M_*/M_\odot =$

^a Conselice & Arnold (2009) have also used galaxy samples at $z \lesssim 3$, and have identified a possible peak of the galaxy merger fraction at $z \simeq 2$ by fitting data points at $z \simeq 0-5$.

^b The $L_{\rm UV}$ range is estimated from the $M_{\rm UV}-M_*$ relations in Paper I.

^c Jiang et al. (2013) include a sample of Ly α emitters.

 $^{^{}m d}$ The value is the total number of SFGs and QGs for the analyses of the rest-frame UV and optical wavelengths. See Table 1.

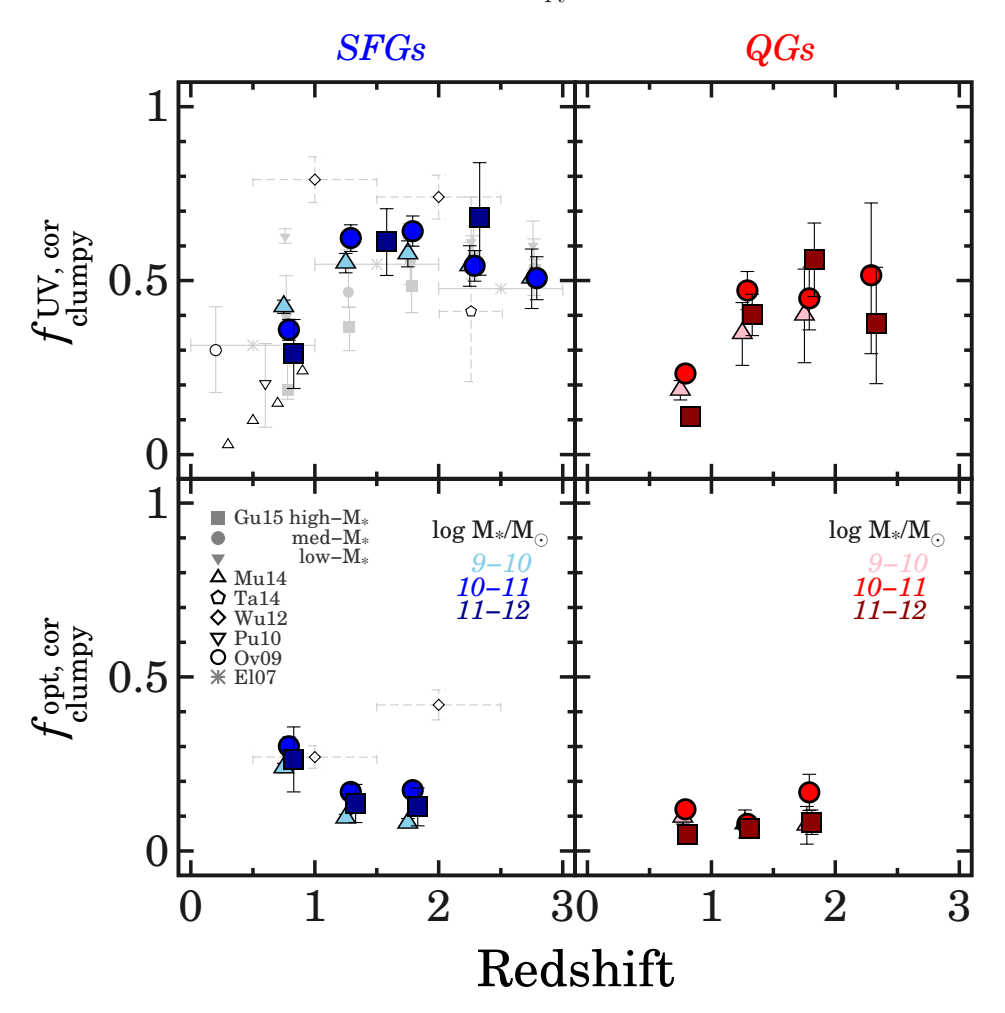


Fig. 3.— Redshift evolution of $f_{\rm clumpy}^{\rm UV,cor}$ (top) and $f_{\rm clumpy}^{\rm opt,cor}$ (bottom) for the photo-z galaxies at $z\simeq 0-3$. The left and right panels indicate $f_{\rm clumpy}^{\rm cor}$ for the SFGs and the QGs, respectively. The filled blue and red symbols denote our $f_{\rm clumpy}^{\rm cor}$ measurements for the SFGs and the QGs in each M_* bin ($\log M_*/M_{\odot} = 9-10$: triangles; 10-11: circles; 11-12: squares). The error bars are given by Poisson statistics from the galaxy number counts. The gray symbols show $f_{\rm clumpy}$ in the literature (asterisks: Elmegreen et al. 2007; open circle: Overzier et al. 2010; inverse triangle: Puech 2010; diamonds: Wuyts et al. 2012; pentagon: Tadaki et al. 2014; triangles: Murata et al. 2014; gray filled inverse triangles, circles, and squares: galaxies with $\log M_*/M_{\odot} = 9-9.8$, 9.8-10.6, and 10.6-11.4, respectively, in Guo et al. 2015). The error bars are put by Poisson statistics from the galaxy number counts if the reference does not show uncertainties of $f_{\rm clumpy}$. Note that our SFGs and QGs are classified by the sSFR value, \log sSFR = 0.1 Gyr⁻¹. This sSFR criterion would include galaxies with a moderately high sSFR in our QG sample (see also, Section 6.1.1).

 $10-11,\,f_{\rm clumpy}^{\rm UV,cor}$ has $\simeq 50\%$ at $z\simeq 2-3,$ and then drops to $\simeq 40\%$ at $z\simeq 0$. In a low- M_* bin of $\log M_*/M_\odot=9-10,\,f_{\rm clumpy}^{\rm UV,cor}$ are an approximately constant value of $f_{\rm clumpy}^{\rm UV,cor}\simeq 50-60\%$ at $z\simeq 1-3,$ and slightly decreases to $\simeq 40\%$ at $z\simeq 0$. In contrast, $f_{\rm clumpy}^{\rm opt,cor}$ shows small values, $\simeq 10-30\%,$ at $z\simeq 0-3$ compared to $f_{\rm clumpy}^{\rm UV,cor}$. There is no significant dependence of $f_{\rm clumpy}^{\rm opt,cor}$ on M_* .

no significant dependence of $f_{\rm clumpy}^{\rm opt,cor}$ on M_* . For the QGs, the evolutional $f_{\rm clumpy}^{\rm UV,cor}$ trends are similar to those of the SFGs. Even in the similarity of the $f_{\rm clumpy}^{\rm UV,cor}$ evolution, $f_{\rm clumpy}^{\rm UV,cor}$ for the QGs are typically smaller than those for the SFGs by a factor of $\simeq 1.4$. The $f_{\rm clumpy}^{\rm UV,cor}$ values for the QGs gradually decrease from $\simeq 30-50\%$ at $z\simeq 3$ to $\simeq 10-30\%$ at $z\simeq 0$. The relatively high $f_{\rm clumpy}^{\rm UV,cor}$ values could be explained by a high sSFR for our

QGs (see also, Section 6.3). The average sSFR value is $\log {\rm sSFR} \simeq -1.8$ for our QGs at $z\simeq 1-2$. The high sSFR indicates that our QGs have not been completely quenched. In contrast, $f_{\rm clumpy}^{\rm opt,cor}$ for the QGs has small values of $\simeq 10-20\%$ at $z\simeq 0-2$ in all the M_* bins. We find no significant dependence of both $f_{\rm clumpy}^{\rm UV,cor}$ and $f_{\rm clumpy}^{\rm opt,cor}$ on M_* for the QGs. Following the small statistics of the optical clumps, we mainly focus on UV clumps (e.g. $f_{\rm clumpy}^{\rm UV}$) in Sections 6.2, 6.3 and 6.4.

Figure 4 shows $f_{\rm clumpy}^{\rm UV,cor}$ for the $z\simeq 4-8$ LBGs with a UV luminosity of $L_{\rm UV}=0.3-1L_{z=3}^*$, where $L_{z=3}^*$ is the characteristic UV luminosity of LBGs at $z\simeq 3$ ($M_{\rm UV}=-21$; Steidel et al. 1999). Note that $f_{\rm clumpy}^{\rm opt}$ is not presented due to the lack of HST filters covering the rest-frame optical wavelengths at $z\gtrsim 3$. As shown in Figure 4, we find that $f_{\rm clumpy}^{\rm UV,cor}$ remains roughly constant

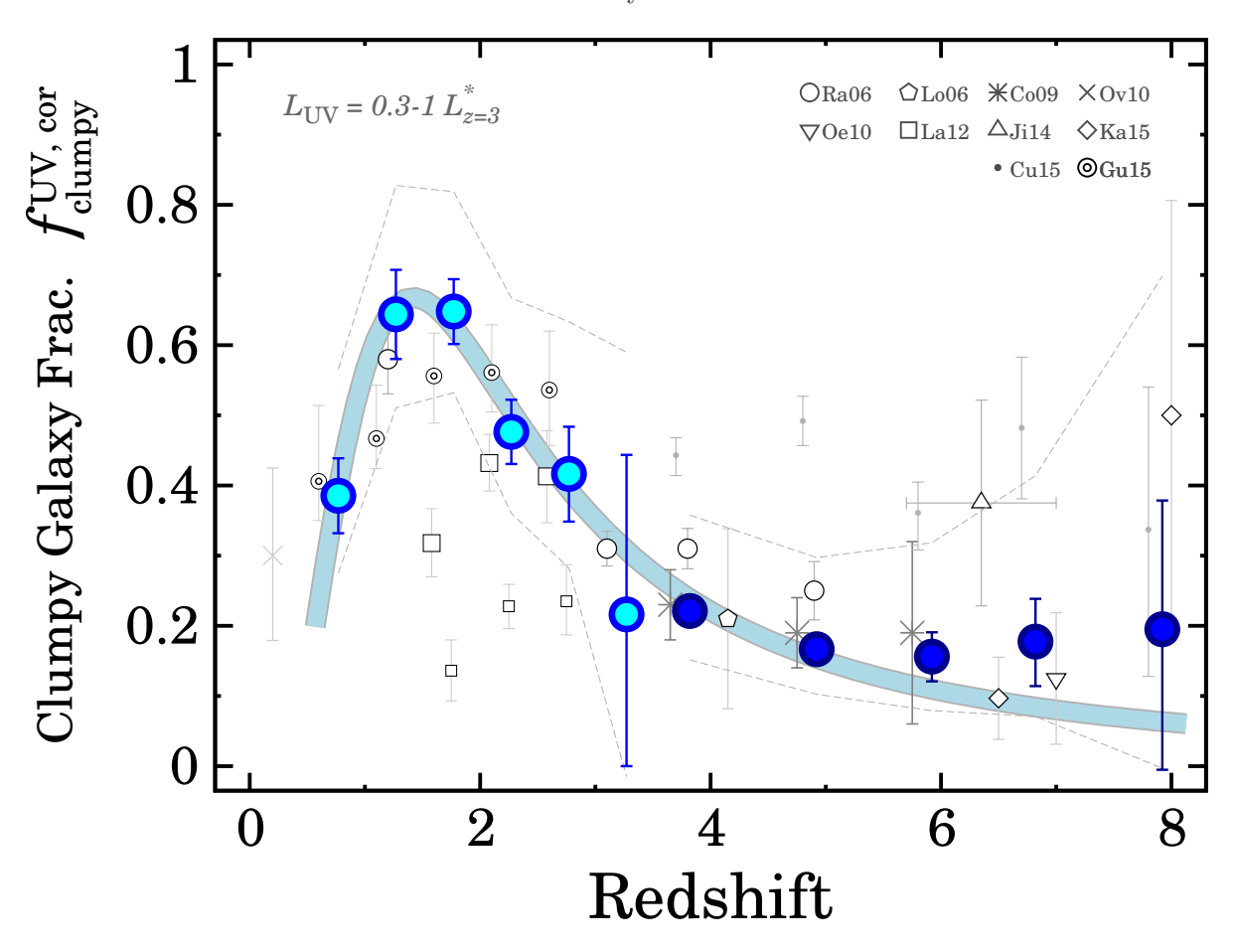


Fig. 4.— Redshift evolution of the clumpy galaxy fraction, $f_{\rm clumpy}^{\rm UV,cor}$, at $z\simeq 0-8$ for the star-forming galaxies with $L_{\rm UV}=0.3-1L_{z=3}^*$. The filled cyan and blue circles denote the SFGs and the LBGs, respectively. The error bars are given by Poisson statistics from the galaxy number counts. The cyan solid curve denotes the best-fit formula of $f_{\rm clumpy}^{\rm UV,cor}(z)=(a+bz)/[1+(z/c)^d]$, where a,b,c, and d are free parameters (Cole et al. 2001). The gray dashed lines present the upper and lower limits of $f_{\rm clumpy}^{\rm UV,cor}$ derived by changing F_c in a range of $0.5\times F_c^{\rm fid}-2\times F_c^{\rm fid}$, where $F_c^{\rm fid}$ is the fiducial F_c value for each redshift. The gray symbols show LBAs and LBGs with clumps or irregular morphologies in the literature (open circles: Ravindranath et al. 2006; pentagon: Lotz et al. 2006; asterisks: Conselice & Arnold 2009; inverse triangle: Oesch et al. 2010; cross: Overzier et al. 2010; open squares: Law et al. 2012b; triangle: Jiang et al. 2013; diamonds: Kawamata et al. 2014; dots: Curtis-Lake et al. 2014). The small and large open squares are based on the selection of clumpy galaxies with the GM_{20} and A indices, respectively. The double circles represent $f_{\rm clumpy}^{\rm UV,cor}$ for SFGs with $\log M_*/M_{\odot}=9.6-10.4$ in Guo et al. (2015). The error bars are given by Poisson statistics from the number of sample galaxies, if no error bar has been presented in the literature.

around $\simeq 20\%$ for the LBGs at $z \simeq 4-8$ albeit with the large error bars at $z \gtrsim 6$.

6.1.2. Comparisons of f_{clumpy} between our Photo-z Galaxies and Previous Studies

We compare our $f_{\rm clumpy}$ for the photo-z galaxies with those of previous studies at $z \simeq 0-3$ in Figure 3. Table 2 summarizes previous studies on clumpy galaxies at $z \simeq 0-3$. The $f_{\rm clumpy}$ data points and the error bars of these previous studies are taken from Guo et al. (2015). In most cases, our clump identification method is slightly different from those of these previous studies (see Table 2). We hereafter specify the methods in the following comparisons for several of these studies.

The clumpy structures have widely been investigated for star-forming galaxies at the rest-frame UV wavelength. Elmegreen et al. (2007) have reported that $f_{\rm clumpy}^{\rm UV}$ is $\simeq 50-60\%$ at $z\simeq 2-3$ and $\simeq 30\%$ at $z\simeq 0-1$ using a sample of 1003 starburst galaxies.

Puech (2010) have found $f_{\rm clumpy}^{\rm UV} \simeq 20\%$ at $z \simeq 0.6$ for 63 emission-line galaxies. Overzier et al. (2010) have obtained $f_{\rm clumpy}^{\rm UV} \simeq 20\%$ for 30 Lyman break analogues (LBAs) at $z \simeq 0.2$ which is a low-z UV bright galaxy population (see also, Guaita et al. 2015). Tadaki et al. (2014) have examined clumpy structures for 100 H\$\alpha\$ emitters (HAEs) at $z \simeq 2.2 - 2.5$, and have obtained $f_{\rm clumpy}^{\rm UV} \simeq 40\%$. Wuyts et al. (2012) have measured $f_{\rm clumpy}^{\rm UV}$ to be $\simeq 70 - 80\%$ at $z \simeq 0.5 - 2.5$ based on a sample of 649 star-forming galaxies. Murata et al. (2014) have identified clumpy structures among 24027 galaxies at $z \simeq 0 - 1$ in COSMOS, suggesting a gradual decrease from $f_{\rm clumpy} \simeq 20\%$ at $z \simeq 1$ to $\simeq 0\%$ at $z \simeq 0$. Recently, Guo et al. (2015) have investigated clumpy structures of 3229 SFGs in the UDS and GOODS-S data for the evolution of $f_{\rm clumpy}^{\rm UV}$ at $z \simeq 0 - 3$. In a M_* bin of $\log M_*/M_\odot = 9 - 9.8$, Guo et al.'s $f_{\rm clumpy}^{\rm UV}$ show no evo-

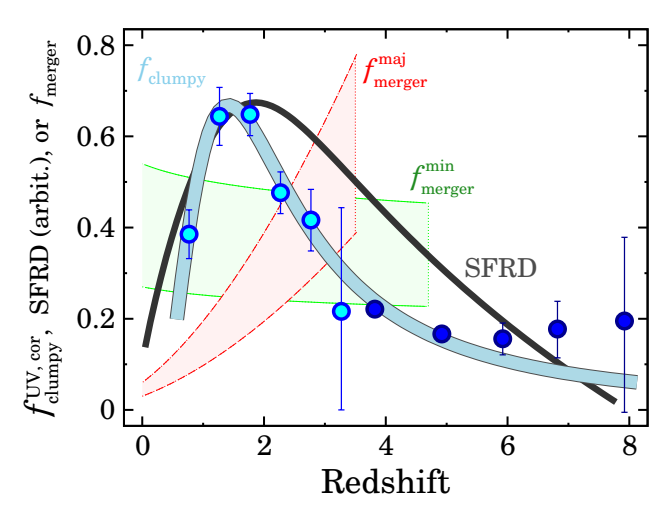


FIG. 5.— Same as Figure 4, but for the comparisons with the cosmic SFR density (the black solid line; Madau & Dickinson 2014) and merger fractions (the shaded regions; Lotz et al. 2011). The red and green shaded regions present the galaxy major and minor merger fractions, $f_{\rm merger}^{\rm maj}$ and $f_{\rm merger}^{\rm min}$, respectively, assuming that the merger observability timescale ranges from 1 to 2 Gyr. The cosmic SFR density is arbitrarily shifted and scaled along the y axis.

lution, $\simeq 60\%$, at $\simeq 0-3$. In contrast, $f_{\rm clumpy}^{\rm UV}$ gradually decreases from $\simeq 60\%$ at $z\simeq 3$ to $\simeq 10-30\%$ at $z\simeq 0$ in M_* bins of $\log M_*/M_\odot=9.8-10.6$ and 10.6-11.4. The evolutional $f_{\rm clumpy}^{\rm UV}$ trends of these studies are roughly consistent with our $f_{\rm clumpy}^{\rm UV,cor}$ measurements at $z\simeq 0-3$.

On the other hand, a few of previous studies have derived $f_{\rm clumpy}^{\rm opt}$ for star-forming galaxies (e.g. Förster Schreiber et al. 2011; Wuyts et al. 2012). Wuyts et al. (2012) have measured $f_{\rm clumpy}^{\rm opt}$ for 649 star-forming galaxies at $z\simeq 2-3$ in addition to $f_{\rm clumpy}^{\rm UV}$. Our measurement is remarkably consistent with $f_{\rm clumpy}^{\rm opt}$ of Wuyts et al. (2012) at $z\simeq 1$. However, $f_{\rm clumpy}^{\rm opt}$ are smaller than theirs at $z\simeq 2$ by a factor of three. This discrepancy might result from the difference of clump identification methods.

These comparisons indicate that our $f_{\rm clumpy}$ measurements at $z \simeq 0-3$ are consistent with the results of the previous studies. The $f_{\rm clumpy}$ agreements ensure the reliability of our clumpy structure analyses.

6.1.3. Comparisons of f_{clumpy} between our LBGs and Previous Studies

We compare our $f_{\rm clumpy}^{\rm UV,cor}$ values for the LBGs with results of previous studies on UV-bright galaxies at $z\gtrsim 4$. In Figure 4, we plot $f_{\rm clumpy}^{\rm UV}$ for UV-bright galaxies with a UV luminosity range of $L_{\rm UV}\simeq 0.3-1L_{z=3}^*$ similar to ours (see Table 2). All of these UV-bright galaxies have been selected in the dropout technique (Steidel et al. 1999). Several of these studies aim to search for merger-like systems to derive the galaxy merger fractions. It is interesting to compare our "clumpy" galaxies with "merger-like" systems in these previous studies due to the morphological similarity. Here we refer all of these LBGs with irregular morphologies as "clumpy" galaxies. Lotz et al. (2006) have derived a clumpy fraction of $f_{\rm clumpy}^{\rm UV}\simeq 21\%$ for LBGs at $z\simeq 4$ based on the GM_{20}

criterion (see the caption of Table 2). Ravindranath et al. (2006) have obtained a roughly constant value of $f_{\rm clumpy}^{\rm UV} \simeq 20-30\%$ for 1333 LBGs at $z\simeq 3-5$ in the Sérsic profile fitting. Conselice & Arnold (2009) have measured $f_{\text{clumpy}}^{\text{UV}}$ using the A index, and have obtained $f_{\rm clumpy}^{\rm UV} \simeq 20\%$ at $z \simeq 3-5$. Oesch et al. (2010) have found two clumpy objects among 21 LBGs at $z \simeq 7$, corresponding to $f_{\rm clumpy}^{\rm UV} \simeq 10\%$, identified by visual inspection. Jiang et al. (2013) have suggested $f_{\rm clumpy}^{\rm UV} \simeq 40\%$ given by visual inspections for LAEs and LBGs at $z \simeq 5-7$. Kawamata et al. (2014) have found $f_{\rm clumpy}^{\rm UV} \simeq 10\%$ at $z \simeq 6-7$ and $\simeq 50\%$ at $z \simeq 8$, by visual inspection, for LBG samples selected in two HFF fields. These $f_{\rm clumpy}^{\rm UV}$ values are remarkably comparable to our results albeit with relatively large error bars at $z\gtrsim 6$. The $f_{\rm clumpy}^{\rm UV}$ agreements with the results of the visual inspections encourage our automated method for faint sources at $z \gtrsim 6$.

On the other hand, we find that our $f_{\rm clumpy}^{\rm UV}$ values are smaller than those of LBGs at $z\simeq 4-8$ in Curtis-Lake et al. (2014). As described in Section 6.3.2, $f_{\rm clumpy}^{\rm UV}$ depends on the UV luminosity. The sample galaxies of Curtis-Lake et al. (2014) would be slightly brighter than the range of $L_{\rm UV}=0.3-1L_{z=3}^*$. Indeed, Curtis-Lake et al. (2014) have obtained an $r_{\rm e}$ evolution, which also depends on $L_{\rm UV}$, different from ours (see Paper I). We thus attribute the $f_{\rm clumpy}^{\rm UV}$ difference to the $L_{\rm UV}$ range.

6.1.4. Evolution of Clumpy Fractions at $z \simeq 0-8$

We present the redshift evolution of $f_{\rm clumpy}^{\rm UV}$ at $z\simeq 0-8$ in a compilation of the photo-z galaxy and LBG samples. Figure 4 shows $f_{\rm clumpy}^{\rm UV,cor}$ for SFGs and LBGs with $L_{\rm UV}=0.3-1L_{z=3}^*$. We find that the $f_{\rm clumpy}^{\rm UV,cor}$ value is in good agreement between the SFGs at $z\simeq 3.5$ and the LBGs at $z\simeq 4$. This $f_{\rm clumpy}^{\rm UV,cor}$ agreement suggests that the difference of galaxy selections (i.e. photo-z or Lyman break) would minimally affect the $f_{\rm clumpy}^{\rm UV,cor}$ evolution. This argument is also supported by the evolution of galaxy sizes using the photo-z and LBG samples same as those of this study. (Paper I).

We identify an evolutional trend that $f_{\rm clumpy}^{\rm UV}$ increases from $z\simeq 8$ to $\simeq 1-3$ and subsequently decreases from $z\simeq 1$ to $\simeq 0$. This $f_{\rm clumpy}^{\rm UV,cor}$ trend is similar to the "Madau-Lilly" plot of the cosmic SFR density (SFRD) evolution (e.g., Madau et al. 1996; Lilly et al. 1996; Madau & Dickinson 2014). As shown in Figure 4, the $f_{\rm clumpy}^{\rm UV,cor}$ evolution is well described by the Madau-Lilly plot-type formula of $f_{\rm clumpy}^{\rm UV,cor}(z)=(a+bz)/[1+(z/c)^d]$, where a,b,c, and d are free parameters (Cole et al. 2001). The best-fit function of $f_{\rm clumpy}^{\rm UV,cor}(z)$ indicates the presence of an $f_{\rm clumpy}^{\rm UV,cor}$ peak at $z\simeq 1-2$. Figure 5 compares the best-fit $f_{\rm clumpy}^{\rm UV,cor}$ function with the cosmic SFRD in Madau & Dickinson (2014). This comparison suggests the evolutional similarity between $f_{\rm clumpy}^{\rm UV,cor}$ and the cosmic SFRD albeit with a possible redshift difference of the peaks. Our self-consistent analyses for clumpy structures

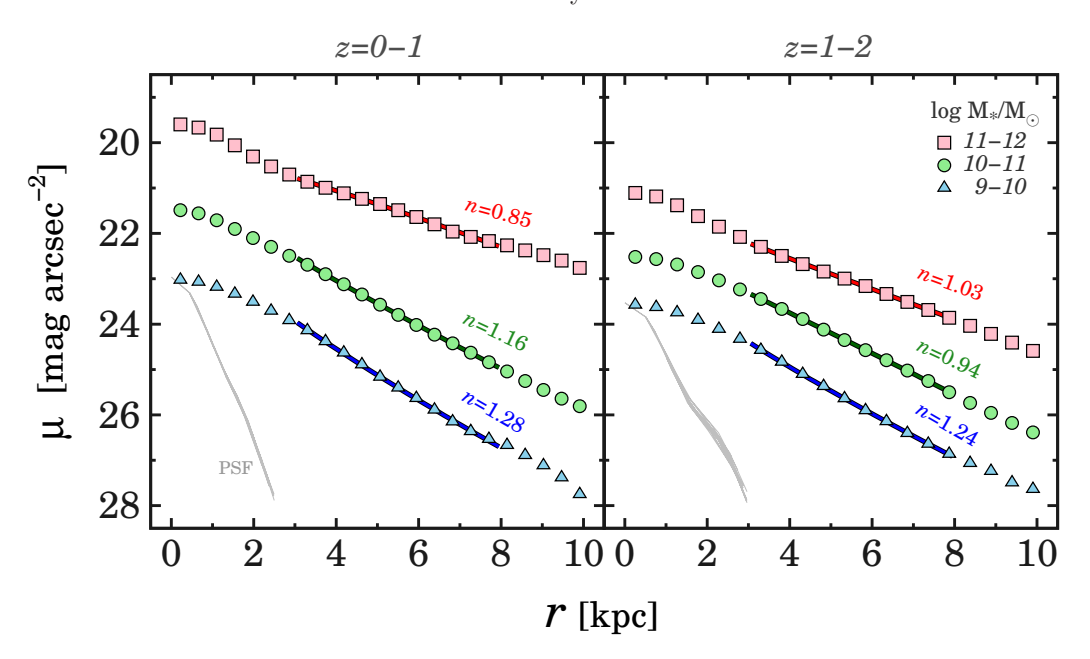


Fig. 6.— Radial SB profiles of clumpy galaxies at z = 0 - 1 (left) and z = 1 - 2 (right) in the median stacked images at the rest-frame optical wavelength. The blue triangles, green circles, and red squares represent radial SB profiles in the bins of $\log M_*/M_{\odot} = 9 - 10, 10 - 11,$ and 11 - 12, respectively. The error bars of each data point are smaller than the size of symbols. The colored curves indicate the best-fit Sérsic functions to each radial SB profile at r = 3 - 8 kpc with the color coding the same as for the symbols. The gray lines denote the PSFs of the J_{125} (left) and H_{160} (right) images.

TABLE 3 THE BEST-FIT SÉRSIC INDICES FOR THE RADIAL SB PROFILES OF CLUMPY GALAXIES

Redshift	Sérsic index n					
(4)		$\log M_*/M_{\odot} = 10 - 11$	$\log M_*/M_{\odot} = 11 - 12$			
(1)	(2)	(3)	(4)			
0 - 1	0.85 ± 0.13	1.16 ± 0.06	1.28 ± 0.11			
1 - 2	1.03 ± 0.07	0.94 ± 0.03	1.24 ± 0.08			

NOTE. — Columns: (1) Redshift. (2)-(4) Best-fit Sérsic indices of the radial SB profiles for the photo-z galaxies with $\log M_*/M_{\odot} = 9 - 10$, 10 - 11, and 11 - 12, respectively.

at $z \simeq 0-8$ enable us to discover, for the first time, the

evolutional trend and the peak of $f_{\rm clumpy}^{\rm UV}$.

For comparison, we plot $f_{\rm clumpy}^{\rm UV}$ in previous studies on UV-bright galaxies at $z \simeq 1-3$ where the $f_{\rm clumpy}^{\rm UV}$ peak is shown in our sample in Figure 4. Ravindranath et al. (2006) have analyzed 153 starburst galaxies with $L_{\rm UV} \simeq 0.3-1$ and have obtained $f_{\rm clumpy}^{\rm UV} \simeq 60\%$ at $z\simeq 1.2.$ The $f_{\rm clumpy}^{\rm UV}$ value is in remarkably good agreement with our $f_{\text{clumpy}}^{\text{UV}}$ measurements. Law et al. (2012b) have selected clumpy objects among BX/BM galaxies and LBGs at $z \sim 2-3$ using two selection criteria based on GM_{20} and A indices. We find that the A-based $f_{\rm clumpy}^{\rm UV}$ is consistent with ours at $z\simeq 3$, but more quickly drops at $z\lesssim 2$ than our $f_{\rm clumpy}^{\rm UV,cor}$ evolution. The GM_{20} -based $f_{
m clumpy}^{
m UV}$ measurements show a lower values of $f_{\rm clumpy}^{\rm UV} \simeq 20-30\%$ at $z\simeq 2-3$ than ours. We do not reveal an exact cause for producing the $f_{\rm clumpy}^{\rm UV}$ differences. We guess that the $f_{\text{clumpy}}^{\text{UV}}$ difference may be caused by the combination of the $L_{\rm UV}$ range and clump detection methods.

To enlarge the number of data points at $z \simeq 1$ – 3, we re-plot $f_{\rm clumpy}^{\rm UV,cor}$ of the Guo et al.'s SFGs with $\log M_*/M_\odot = 9.8-10.6$ (see Figure 3). The Guo et al.'s $f_{\rm clumpy}^{\rm UV,cor}$ has been measured in the M_* -limited sample. Despite the difference of the galaxy selection methods, this M_* range roughly corresponds to $L_{\rm UV} \simeq 0.3 - 1L_{z=3}^*$ according to the $M_{\rm UV}$ - M_* relation (Paper I). As shown in Figure 4, the $f_{\rm clumpy}^{\rm UV}$ in Guo et al. (2015) follows our $f_{\rm clumpy}^{\rm UV,cor}$ evolution at $z \simeq 0-3$. These previous studies of f_{clumpy}^{UV} support that the peak of f_{clumpy}^{UV} possibly exist at $z \simeq 1-3$.

6.1.5. Is the f_{clumpy} Peak Real?

We examine whether the possible $f_{\rm clumpy}^{\rm UV}$ peak at $z\simeq$ 1-3 is real. Basically, high spatial resolution and high sensitivity data are required to detect clumps in high-z galaxies. In the limited spatial resolution and sensitivity of HST, a low detection completeness for clumps at $z \gtrsim 4$ might produce an $f_{\rm clumpy}^{\rm UV}$ peak at $z \simeq 1-3$. Here we discuss five potential systematics that may produce an $f_{\text{clumpy}}^{\text{UV}}$ peak: the differences of 1) the spatial resolu-

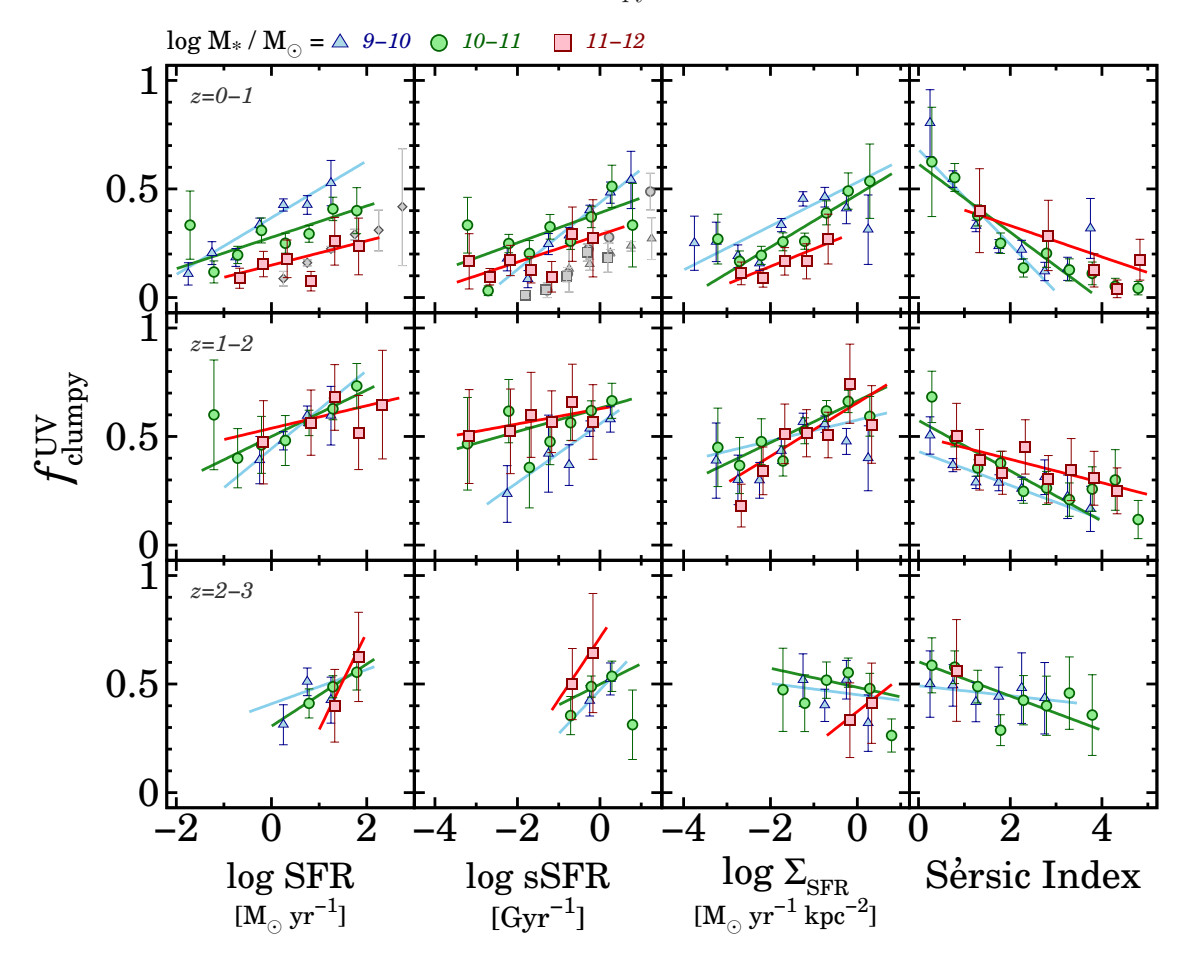


Fig. 7.— Dependences of $f_{\rm clumpy}^{\rm UV}$ on physical quantities (SFR, sSFR, $\Sigma_{\rm SFR}$, and n from left to right) for the photo-z galaxies. The top, middle, and bottom panels indicate the redshift bins of z=0-1, 1-2, and 2-3, respectively. The cyan triangles, green circles, and red squares denote $f_{\rm clumpy}^{\rm UV}$ for galaxies with $\log M_*/M_\odot=9-10$, 10-11, and 11-12, respectively. The colored lines indicate the best-fit linear function to $f_{\rm clumpy}^{\rm UV}$ in each M_* bin with the color coding the same as for the symbols. The gray symbols are $f_{\rm clumpy}$ at z=0.6-0.8 in Murata et al. (2014) (diamonds: $\log M_*/M_\odot>9.5$; triangles: $\log M_*/M_\odot=9.5-10$; circles: $\log M_*/M_\odot=10.5-11$).

tion, 2) clump search areas, 3) selection criteria of sample galaxies, 4) clump identification methods, and 5) the cosmological SB dimming effects between the SFGs at $z \lesssim 3$ and the LBGs at $z \gtrsim 4$.

- 1. Spatial resolution we check whether the difference in the spatial resolution changes $f_{\rm clumpy}^{\rm UV}$. In Section 4, we have used the coadded images to select clumpy LBGs. Here we measure $f_{\rm clumpy}^{\rm UV}$ for the LBGs at $z\simeq 4$ with the I_{814} images whose PSF size is $\simeq 2$ times smaller than that of the coadded images. The I_{814} band covers the rest-frame wavelengths slightly bluer than that of the coadded images. Even in the wavelength shift, we find a good agreement in the $f_{\rm clumpy}^{\rm UV}$ values between the I_{814} and coadded images (i.e. $f_{\rm clumpy}^{\rm UV}=0.146\pm0.012$ and 0.147 ± 0.025 for the I_{814} and coadded images, respectively). This agreement indicates that the difference in the spatial resolution is unlikely to produce the $f_{\rm clumpy}^{\rm UV}$ peak.
- 2. Clump search areas we test whether $f_{\rm clumpy}^{\rm UV}$ is affected by the difference in the clump search areas. In Section 4, we have searched for clumps in areas defined by the segmentation maps. There is a possibility that clumps at outer galactic regions are not identified by small segmentation areas for high-z compact sources. Here we enlarge the segmentation areas by a factor of $\simeq 2$ and measure $f_{\rm clumpy}^{\rm UV}$ for the LBGs at $z\simeq 4$. We find that $f_{\rm clumpy}^{\rm UV}$ changes within $\simeq \pm 5\%$ in the large clump search area. This test suggests that the difference in clump search areas does not significantly affect the $f_{\rm clumpy}^{\rm UV}$ values.
- 3. Selection criteria of sample galaxies we examine whether $f_{\rm clumpy}^{\rm UV}$ is changed by the different selection criteria of sample galaxies. In Section 3, the sample LBGs have been selected only by the $m_{\rm UV}$ criterion to improve the statistics at $z\gtrsim 6$. Here we re-select LBGs in the selection criteria similar to those for the SFGs (i.e., the cuts of $R_{\rm e,major}$, H_{160} magnitude, and q), and measure $f_{\rm clumpy}^{\rm UV}$ at

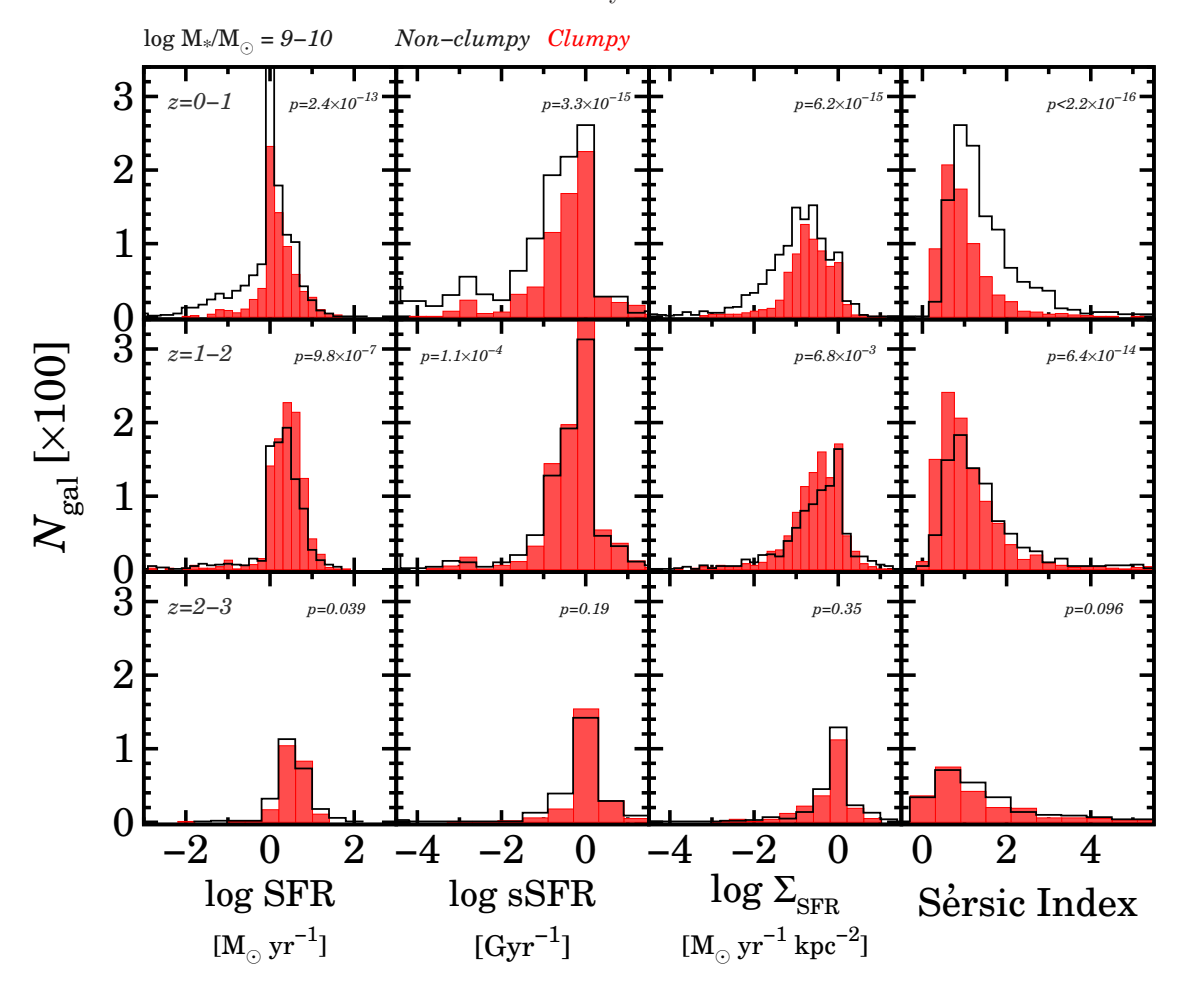


FIG. 8.— Number distributions of clumpy (filled red) and non-clumpy (open black) galaxies with respect to physical quantities (SFR, sSFR, $\Sigma_{\rm SFR}$, and n from left to right) for the photo-z galaxies with $\log M_*/M_{\odot} = 9-10$. Each row, from top to bottom, denotes galaxies in a redshift bin of z=0-1, z=0, and z=0, respectively. The number in each panel represents z=0-values of K-S tests (see Section 6.3 for details).

- $z\simeq 4.$ This sample selection significantly reduces the number of the LBGs at $z\simeq 4.$ Nevertheless, we find that $f_{\rm clumpy}^{\rm UV}$ does not significantly change.
- 4. Clump identification methods we test whether the difference in the clump identification methods affects $f_{\rm clumpy}^{\rm UV}$. In Section 3, we have not used the $d_{\rm cl}/r_{\rm e}$ criterion to identify clumpy LBGs. Here we include the $d_{\rm cl}/r_{\rm e}$ criterion in the selection for clumpy LBGs at $z\simeq 4$, and measure $f_{\rm clumpy}^{\rm UV}$. We obtain $f_{\rm clumpy}^{\rm UV}=0.2\pm0.1$ that agrees with the old $f_{\rm clumpy}^{\rm UV,cor}$ value within a 1σ error. This agreement confirms that $f_{\rm clumpy}^{\rm UV}$ is not largely changed by the clump identification methods.
- 5. Cosmological SB dimming effects we investigate how the cosmological SB dimming effects affect $f_{\rm clumpy}^{\rm UV}$. In the previous sections, we have corrected F_c for the $f_{\rm clumpy}^{\rm UV}$ measurements. The F_c correction takes into account the cosmological SB dimming effects. However, one might expect that the evolutional $f_{\rm clumpy}^{\rm UV}$ trends strongly depend on

the F_c values. Here we demonstrate the effect of the F_c variation on $f_{\rm clumpy}^{\rm UV,cor}$ (dashed lines in Figure 4; see the caption). We reproduce a broad peak of $f_{\rm clumpy}^{\rm UV,cor}$ at $z\simeq 1-3$ even in the F_c allowance. Moreover, we should note that typical clumps are reliably identified less affected by the cosmological SB dimming effect than low SB structures.

These tests indicate that the $f_{\rm clumpy}^{\rm UV}$ peak would not be produced by the difficulties of clump identifications at high z. We thus conclude that the $f_{\rm clumpy}^{\rm UV}$ peak is real.

6.2. Radial SB Profiles of Clumpy Galaxies

We investigate structural properties of our clumpy host galaxies. To obtain the underlying components of clumpy galaxies, we construct in the median stacked images of the clumpy galaxies. In general, clumps would be randomly distributed in a host galaxy. The median stacking analysis would allow us to examine the underlying galaxy components negligibly affected by the flux contributions of clumpy structures (e.g., Cassata et al. 2005; Ravindranath et al. 2006; Elmegreen et al. 2007).

Figure 6 presents the radial SB profiles of galaxies with

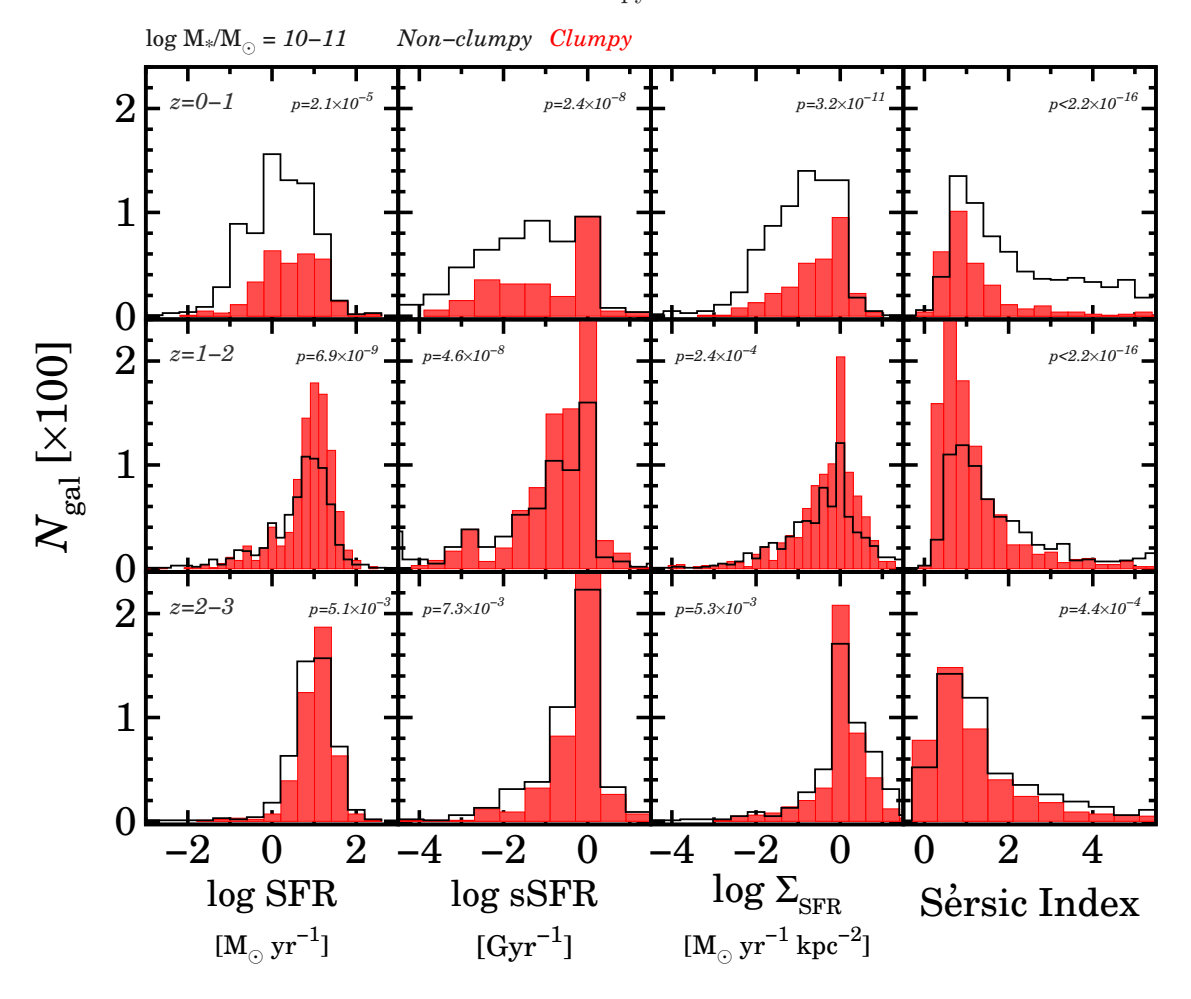


Fig. 9.— Same as Figure 8, but for the photo-z galaxies with $\log M_*/M_{\odot} = 10 - 11$.

UV clumps at $z \simeq 0-2$ in the median stacked images. Here we use the rest-frame optical images less affected by the clumpy structures than the rest-frame UV ones (see $f_{\rm clumpy}^{\rm opt}$ in Section 6.1). The radial SB profiles of clumpy galaxies at $z \gtrsim 2-3$ are not shown in Figure 6. This is because the rest-frame optical wavelength at $z \gtrsim 2-3$ are redshifted beyond the wavelength coverage of WFC3/IR.

The radial SB profiles are obtained in the following processes. First, we align P.A. of individual clumpy galaxies in two-dimensional (2D) images. Next, we normalize the galaxy-light counts by the total magnitude of galaxies. We then stack the 2D images of clumpy galaxies in order to obtain the 2D median radial SB profiles. Finally, we extract one-dimensional (1D) radial SB profiles with a slice of three-pixel width along the major axis. Here we do not mask clumpy structures in the stacking. Even in no masking procedure, the *median* stacking analysis allows us to securely obtain the radial SB profiles of underlying galaxy components. The details of the stacking analysis are found in M. Kubo et al. in preparation. The number of stacked clumpy galaxies are 714, 300, and 36 (1015, 953, and 206), at z = 0 - 1 (z = 1 - 2) in the bins of $\log M_*/M_{\odot} = 9 - 10, 10 - 11, \text{ and } 11 - 12, \text{ respectively.}$

We fit the Sérsic function to the radial SB profiles at

r=3-8 kpc where the PSF broadening effect would be negligible. Table 3 summarizes the best-fit Sérsic indices. The best-fit n values are $n\simeq 1$ for the radial SB profiles in all the M_* and z bins. These low n values indicate that clumpy galaxies tend to have disk-like light profiles.

In Paper I, the n values have been derived in the profile fitting for the entire galaxy regions including the central bulge-like components. In general, the central components tend to have a large n value of $n \gtrsim 2$ for galaxies at $z \simeq 0-2$. For this reason, we have obtained a slightly large value of $n \simeq 1.5$ in Paper I. Here we re-measure the n value including the central region for the radial SB profile fitting. We obtain the best-fit n values of $n \simeq 1$ similar to those found in this section.

6.3. Relations between Clumps and Physical Properties of Host Galaxies

We investigate relations between clumps and physical properties of the photo-z galaxies in Section 6.3.1 and the LBGs in Section 6.3.2.

6.3.1. Results for the Photo-z Galaxies

We first examine physical properties for clumpy photoz galaxies. Here we evaluate three quantities related to star formation (SF), i.e., SFR, sSFR, and $\Sigma_{\rm SFR}$, and a

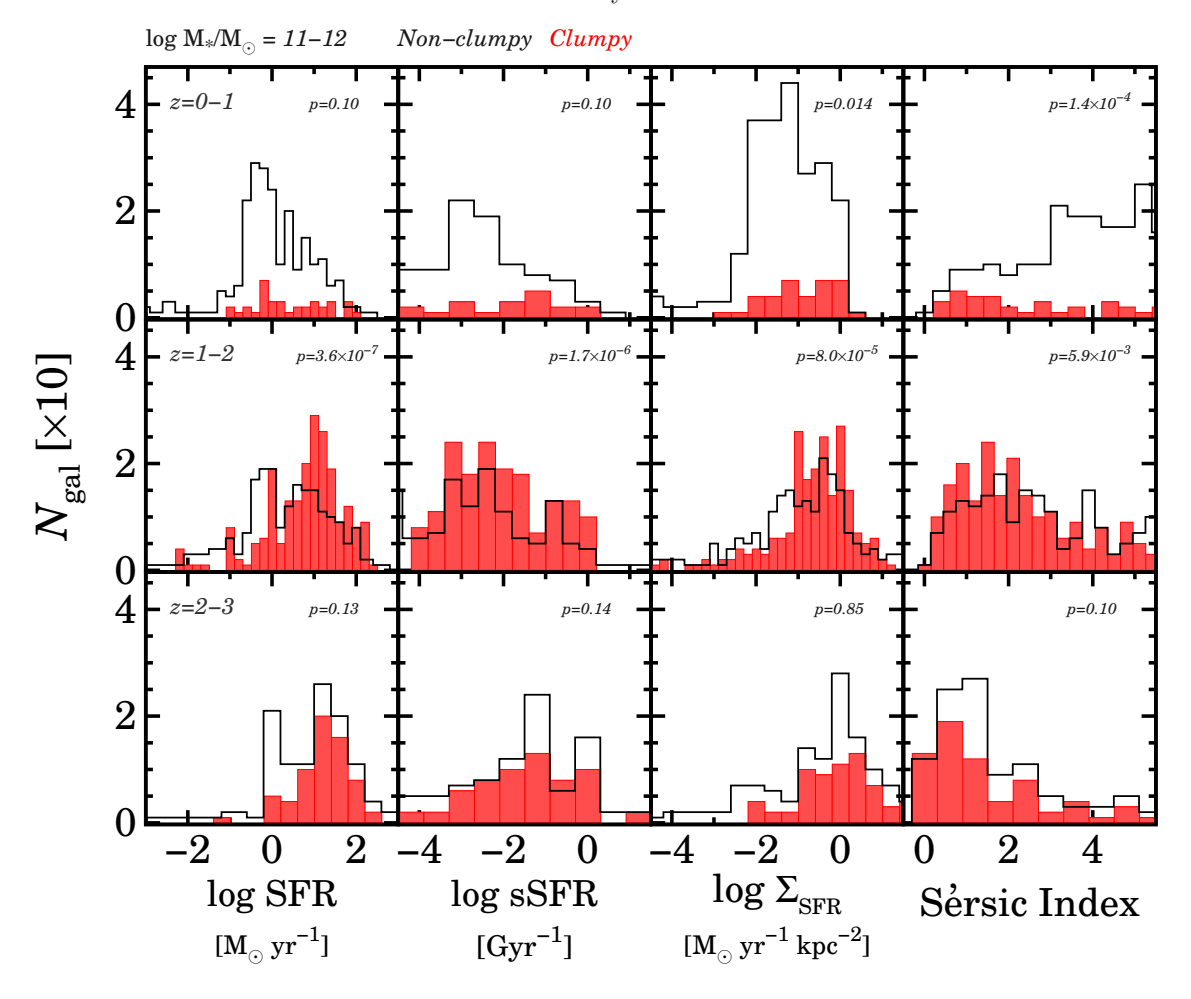


Fig. 10.— Same as Figure 8, but for the photo-z galaxies with $\log M_*/M_{\odot} = 11 - 12$.

structural parameter, n. These quantities are derived from entire fluxes of host galaxies (Skelton et al. 2014, Paper I, Y. Harikane et al. in preparation). In Section 6.2, we have measured n of the radial SB profiles in the stacked images. In this section, we examine n on the individual basis complimentary to the median stacking analysis. To test whether clumps are related to these physical quantities of host galaxies, we employ two approaches: i) to examine dependences of $f_{\rm clumpy}^{\rm UV}$ on physical quantities, and ii) to quantify differences of number distributions between clumpy and non-clumpy galaxies. Approach (i) enables us to clearly identify $f_{\rm clumpy}^{\rm UV}$ trends with respect to physical quantities. Approach (ii) is sensitive to differences of two distributions because of comparisons in a wide dynamic range of physical quantities.

Approach (i) — Figure 7 represents dependences of $f_{\rm clumpy}^{\rm UV}$ on the physical quantities. Here we mainly use the n values derived at the rest-frame optical wavelengths for $z \lesssim 2$, but at the rest-frame UV ones for $z \gtrsim 2$. We find trends that $f_{\rm clumpy}^{\rm UV}$ increases with increasing the three SF-related quantities (i.e., SFR, sSFR, and $\Sigma_{\rm SFR}$) for galaxies in most bins of M_* and z. In contrast, $f_{\rm clumpy}^{\rm UV}$ appears to increase with decreasing n. This $f_{\rm clumpy}^{\rm UV}$ -n re-

lation supports the results of the median stacking analysis in Section 6.2. The correlations tend to be weaker at higher z.

We compare our $f_{\rm clumpy}^{\rm UV}$ relations with those of a previous study. Murata et al. (2014) have reported increasing $f_{\rm clumpy}^{\rm UV}$ trends with SFR and sSFR for star-forming galaxies at $z \simeq 0-1$. As shown in Figure 7, the amplitudes of our $f_{\rm clumpy}$ values are slightly higher than those of Murata et al. (2014). The difference of $f_{\rm clumpy}$ amplitudes would be caused by clump identification methods. Nevertheless, we find that our $f_{\rm clumpy}^{\rm UV}$ trends are comparable to the Murata et al.'s measurements.

Approach (ii) — Figures 8, 9, and 10 compare the number distributions of clumpy and non-clumpy galaxies in the M_* bins of $\log M_*/M_{\odot} = 9 - 10$, 10 - 11, and 11 - 12, respectively. We perform Kolmogorov-Smirnov (K-S) tests to quantify the significance level of differences between the number distributions of clumpy and non-clumpy galaxies. The K-S tests determine probabilities (p-values) of accepting the null hypothesis that two samples are drawn from a statistically identical distribution. If the two distributions are statistically different, the p-values are significantly below $\simeq 5\%$. As shown in p-values in Figures 8, 9, and 10, the K-S tests suggest

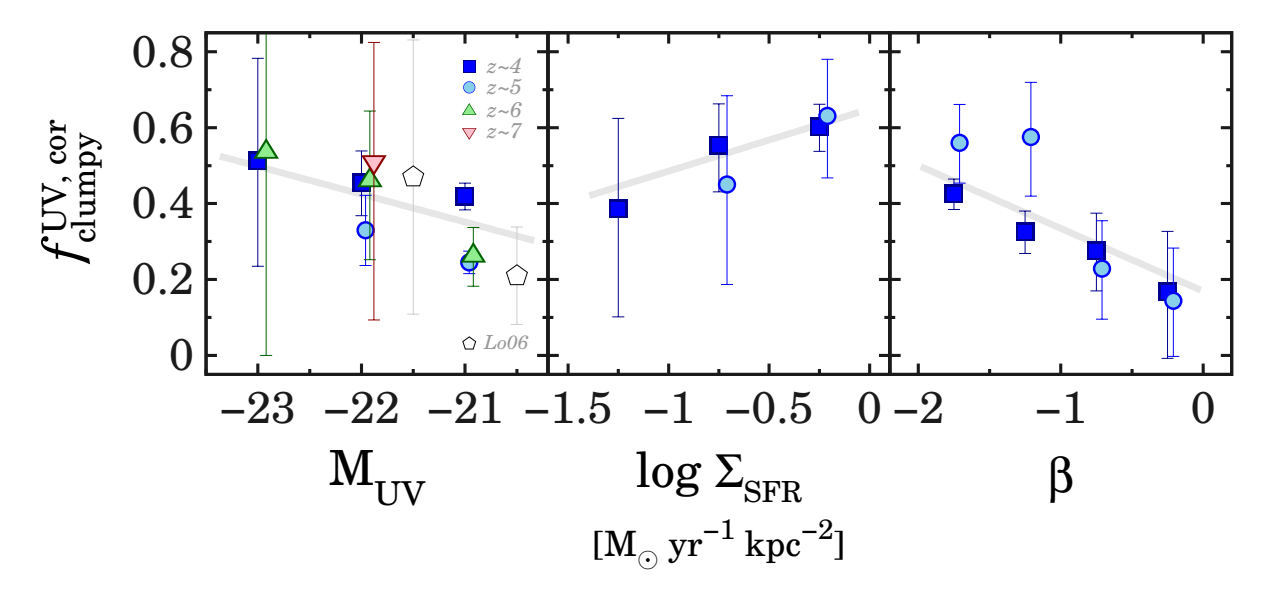


Fig. 11.— Dependence of $f_{\rm clumpy}^{\rm UV,cor}$ on the physical quantities, $M_{\rm UV}$ (left), $\Sigma_{\rm SFR}$ (middle), and β (right), for the LBGs at $z\simeq 4-7$. The relations for $\Sigma_{\rm SFR}$ and β are derived in an $L_{\rm UV}$ range of $L_{\rm UV}=0.3-1L_{z=3}^*$. The blue squares, cyan circles, green triangles and magenta inverse triangle denote the LBGs at $z\simeq 4$, 5, 6 and 7, respectively. The gray lines indicate the best-fit linear functions of $f_{\rm clumpy}^{\rm UV,cor}(x)=ax+b$, where a and b are free parameters. The data points are not shown for LBGs with $F_c<0.2$ and/or $N_{\rm gal}<10$ in the bins of the physical quantities. The open pentagons present $f_{\rm clumpy}^{\rm UV,cor}$ for $z\simeq 4$ LBGs in Lotz et al. (2006).

that the two number distributions of clumpy and non-clumpy galaxies are statistically different in almost all M_* - and z-bins with respect to most physical properties (i.e., $p\ll 5\%$). These results of the K-S tests are compatible with the $f_{\rm clumpy}^{\rm UV}$ trends in Approach (i). However, we obtain a large p-value of $\gtrsim 5\%$ for galaxies in bins of $(\log M_*/M_\odot, z) = (9-10, 2-3), (11-12, 0-1),$ and (11-12, 2-3). Such a high p-value might be attributed to the small statistics of high-z clumpy galaxies.

6.3.2. Results for the LBGs

We next examine physical properties for the clumpy LBGs. We have no measurements of M_* and n for the LBG sample. Instead of M_* and n, we evaluate physical quantities of $M_{\rm UV}$, $\Sigma_{\rm SFR}$, and β for the LBGs. Figure 11 shows dependences of $f_{\rm clumpy}^{\rm UV,cor}$ on physical quantities, $M_{\rm UV}$, $\Sigma_{\rm SFR}$, and β . We perform the F_c corrections to $f_{\rm clumpy}^{\rm UV}$ for the LBG sample. This is because the detection completeness is sensitive strongly to $M_{\rm UV}$ (see Section 5) and weakly to $\Sigma_{\rm SFR}$ and β through weak correlations between $M_{\rm UV}$ and the two quantities of $\Sigma_{\rm SFR}$ and β (e.g., Bouwens et al. 2014a, Paper I). We exclude high SFR SD bins of $\log \Sigma_{\rm SFR} \gtrsim 0~{\rm M}_{\odot}~{\rm yr}^{-1}~{\rm kpc}^{-2}$ dominated by compact LBGs.

In Figure 11, we find a marginal trend that $f_{\rm clumpy}^{\rm UV,cor}$ increases for LBGs with a bright $M_{\rm UV}$, a high $\Sigma_{\rm SFR}$, and a small β (i.e. blue UV slope). According to an empirical relation in Kennicutt (1998), $M_{\rm UV}$ is an indicator of SFR. The $f_{\rm clumpy}^{\rm UV,cor}$ - $M_{\rm UV}$ and $f_{\rm clumpy}^{\rm UV,cor}$ - $\Sigma_{\rm SFR}$ trends for the LBGs are consistent with the correlations for the photo-z galaxies in Section 6.3.1. On the other hand, β is a coarse indicator of the stellar population and dust extinction of galaxies. The vigorous clump formations

would yield young stellar populations on entire galactic regions, producing a blue UV slope. The $f_{\rm clumpy}^{\rm UV,cor}$ - β correlation could be another piece of evidence that clumps are related to the SF activity of host galaxies.

For comparison, we plot LBGs at $z \simeq 4$ in Lotz et al. (2006) in the panel of $f_{\rm clumpy}^{\rm UV,cor}$ - $M_{\rm UV}$ in Figure 11. The detection completeness has been corrected in Lotz et al. (2006). Our $f_{\rm clumpy}^{\rm UV,cor}$ - $M_{\rm UV}$ relation is comparable to that of Lotz et al. (2006).

We quantify the significance level of our $f_{\rm clumpy}^{\rm UV,cor}$ relations. We are not able to apply Approach (ii) in Section 6.3 to the LBG sample due to the small statistics and the differential F_c values depending on $M_{\rm UV}$, $\Sigma_{\rm SFR}$, and β . Instead of Approach (ii), we carry out Spearman rank correlation tests for the $f_{\rm clumpy}^{\rm UV,cor}$ relations in Figure 11. In general, rank correlation tests do not adequately take into account fractional values (e.g. $f_{\rm clumpy}$ in the case of this study) and their error bars. We still expect that the test gives a rough estimate for significance levels of these correlations. We find that the significance levels of these $f_{\rm clumpy}^{\rm UV,cor}$ trends are 4.3σ , 4.9σ , and 4.5σ with respect to $M_{\rm UV}$, $\Sigma_{\rm SFR}$, and β , respectively. The correlation tests suggest that the $f_{\rm clumpy}^{\rm UV,cor}$ correlations are significant with these physical quantities for the LBGs at $z\gtrsim 4$. We have extended the correlation study up to $z\lesssim 7$, and have found the relation between clumps and the SF activity of host galaxies at $z\simeq 0-7$.

6.4. Relations between Clump Colors and Galactocentric Distance

We examine relations between colors and $d_{\rm cl}/r_{\rm e}$ for clumps. Figure 12 presents $m_{\rm UV}-m_{\rm opt}$ colors as a func-

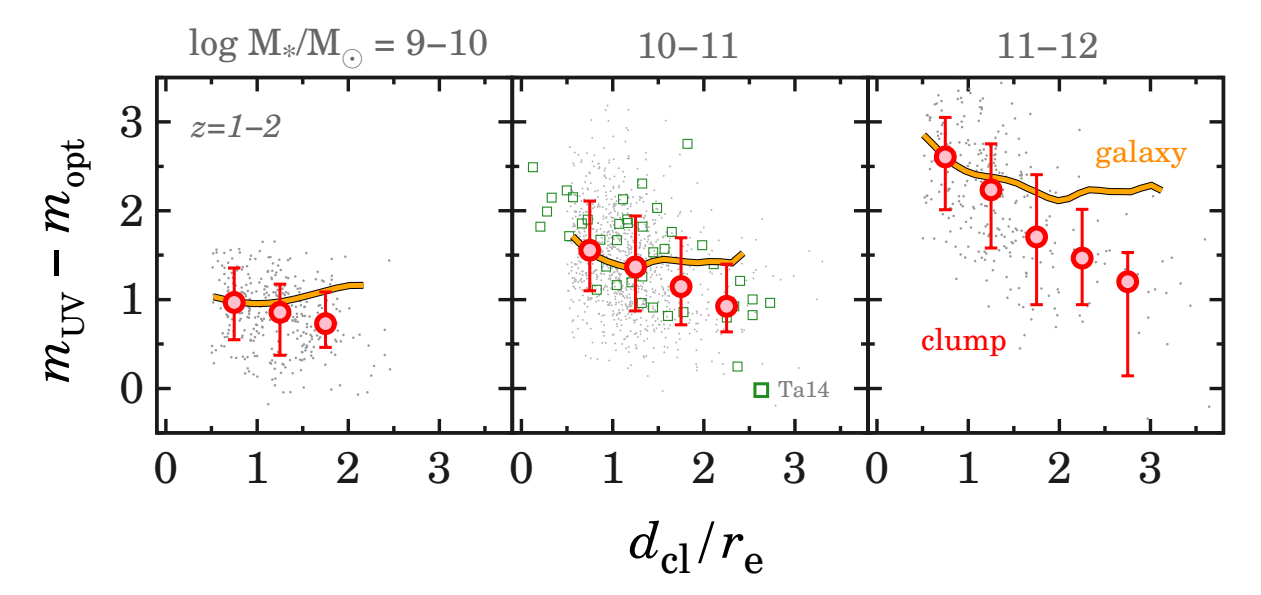


Fig. 12.— Clump $m_{\rm UV}-m_{\rm opt}$ colors as a function of $d_{\rm cl}/r_{\rm e}$ in the M_* bins of $\log M_*/M_{\odot}=9-10$ (left), 10-11 (middle), and 11-12 (right). The gray dots indicate the color measurements for individual clumps. The red circles with error bars represent the median $m_{\rm UV}-m_{\rm opt}$ colors and the 16th and 84th percentiles of the distribution. The orange curves present average galaxy color gradients in each M_* bin. For comparison, the galaxy color gradients are shifted along the y-axis to match the $m_{\rm UV}-m_{\rm opt}$ colors at the reddest median $m_{\rm UV}-m_{\rm opt}$ points. The green squares denote the clump color measurements for HAEs at $z\simeq 2$ (Tadaki et al. 2014) assuming that the galaxy size is $r_{\rm e}=2$ kpc.

tion of $d_{\rm cl}/r_{\rm e}$ for each clump, where $m_{\rm UV}$ and $m_{\rm opt}$ are the magnitudes of UV clumps at the rest-frame UV and optical wavelengths, respectively. Here we measure the $m_{\rm UV}-m_{\rm opt}$ colors in the double-detection mode of SEXTRACTOR after the PSF homogenizations. We obtain $m_{\rm UV}-m_{\rm opt}$ colors at $z\simeq 1-2$ where both $m_{\rm UV}$ and $m_{\rm opt}$ magnitudes are measurable with the HST bands. As shown in Figure 12, we find that the $m_{\rm UV}-m_{\rm opt}$ values tend to be red at a small $d_{\rm cl}/r_{\rm e}$. This color trend is clearly shown for high M_* bins. To evaluate these trends, we perform Spearman rank correlation tests between $m_{\rm UV}-m_{\rm opt}$ and $d_{\rm cl}/r_{\rm e}$. The significance levels of these correlations are 5.1σ , 9.7σ , and 14σ for the mass bins of $\log M_*/M_{\odot}=9-10$, 10-11, and 11-12, respectively.

For comparison, we plot $z\simeq 2$ clumpy HAEs with $\log M_*/M_\odot\simeq 10-11$ in Tadaki et al. (2014). We assume that the galaxy size of these HAEs is $r_{\rm e}=2$ kpc (see the $r_{\rm e}$ evolution in Paper I). We find that our clumpy galaxies have a similar color- $d_{\rm cl}/r_{\rm e}$ correlations to those of these HAEs.

There is a possible source of systematics in which we obtain the clump color- $d_{\rm cl}/r_{\rm e}$ correlations. The background flux of host galaxies is not subtracted in the measurements of the clump magnitudes in Figure 12 and Tadaki et al. (2014). Evolved bright central structures (e.g. bulges) would make a similar color trend of host galaxies to those of clumps (e.g., van Dokkum et al. 2010; Patel et al. 2013; Morishita et al. 2015; Nelson et al. 2015). To show this effect, we compare the typical $m_{\rm UV}-m_{\rm opt}$ color gradients of host galaxies with those of the clump colors in Figure 12. The $m_{\rm UV}-m_{\rm opt}$ colors of host galaxies are derived from the radial SB profiles in the stacked images (Section 6.2). The $m_{\rm UV}-m_{\rm opt}$ uncertainties resulting from the galaxy color variations are typically $\simeq \pm 0.3$ mag (e.g. Guo et al. 2012). As indicated in

Figure 12, the host galaxies show similar color gradients to those of clumps. Nevertheless, we still identify the color- $d_{\rm cl}/r_{\rm e}$ correlations steeper than these galaxy color gradients for the massive bins of $\log M_*/M_\odot = 11-12$ and marginally for $\log M_*/M_\odot = 10-11$. These trends have already been reported in previous studies for massive galaxies (e.g., Förster Schreiber et al. 2011; Guo et al. 2012). In this study, we find, for the first time, the dependence of clump color correlations on M_* .

7. DISCUSSION

7.1. Implications for Clump Formation Mechanisms; Galaxy Mergers or VDI?

We investigate whether our results are consistent with the clump formation mechanisms of galaxy mergers (Section 7.1.1) or VDI (Section 7.1.2). As shown in the following subsections, our results suggest that VDI would be favorable as a clump formation mechanism. In Section 7.2, we discuss the possibility of the clump migration.

7.1.1. Galaxy Mergers?

We first examine the possibility that the galaxy merger is the major clump formation mechanism. In Section 6.1, we identify the $f_{\rm clumpy}^{\rm UV}$ evolution at $z\simeq 0-8$: $f_{\rm clumpy}^{\rm UV}$ increases from $z\simeq 8$ to $z\simeq 3$, and decreases from $z\simeq 1$ to $z\simeq 0$. In the case of the ex-situ clump origin, $f_{\rm clumpy}^{\rm UV}$ should follow the evolution of the merger fraction. Observational studies have measured the galaxy major and minor merger fractions, $f_{\rm merger}^{\rm maj}$ and $f_{\rm merger}^{\rm min}$, at $z\simeq 0-3$, using galaxy close pairs which have a spatial scale of $\simeq 20$ kpc different from the clump-clump separations (e.g., Le Fèvre et al. 2000; Bundy et al. 2009; Bluck et al. 2009; Williams et al. 2011; López-Sanjuan et al. 2013; Man et al. 2012, 2014). In Figure 5, we compare our $f_{\rm clumpy}^{\rm UV}$ evolution with the merger fractions of Lotz et al. (2011)

assuming that these $f_{\rm merger}^{\rm maj}$ and $f_{\rm merger}^{\rm min}$ values continuously evolve beyond $z\simeq 3$. As shown in Figure 5, the evolutional trend of the major merger fraction is probably similar to our $f_{\rm clumpy}^{\rm UV}$ evolution at $z\simeq 0-1$, but is inconsistent beyond $z\simeq 3$. In contrast, the evolutional trend of the minor merger fraction is comparable to our $f_{\rm clumpy}^{\rm UV}$ evolution at $z\gtrsim 3$, but is incompatible at $z\simeq 0-3$. These comparisons indicate that the merger fractions do not explain simultaneously both low-z and high-z trends of our $f_{\rm clumpy}^{\rm UV}$ evolution.

Moreover, numerical simulations predict that the halohalo major and minor merger rates strongly increase from $z \simeq 0$ to $z \simeq 6$, $\propto (1+z)^{2 \sim 3}$ (e.g., Genel et al. 2008, 2009; Fakhouri et al. 2010; Hopkins et al. 2010; Rodriguez-Gomez et al. 2015). Our decreasing $f_{\rm clumpy}^{\rm UV}$ evolution beyond $z \simeq 3$ is also incompatible with the theoretical predictions. Thus, our evolutional $f_{\rm clumpy}^{\rm UV}$ trend is inconsistent with the scenario that the clump formation is mainly driven by galaxy mergers.

7.1.2. *VDI?*

We next examine the possibility that the VDI is the major clump formation mechanism. The Sérsic index of clumpy host galaxies is one of key measurements for distinguishing the clump formation mechanisms. The VDI requires host galaxies to have disk-like underlying components. In Sections 6.2 and 6.3, we have obtained a low Sérsic index of $n \simeq 1$ in the SB profiles of clumpy galaxies. These low n values support that clumpy galaxies tend to have disk-like structures.

tend to have disk-like structures. ⁹
The $f_{\rm clumpy}^{\rm UV}$ is another key measurement. As described below, our $f_{\rm clumpy}^{\rm UV}$ evolution at $z\simeq 0-8$ is consistent with the clump formation mechanism of VDI. The instability of galaxy disks could be sustained by the cold gas accretion as a result of continuous gas supply (e.g., Birnboim & Dekel 2003; Kereš et al. 2005, 2009, 2012; Dekel & Birnboim 2006; Dekel et al. 2009a,b; Nelson et al. 2013). If clumps have the in-situ origin, $f_{\text{clumpy}}^{\text{UV}}$ is expected to evolve with the cold gas accretion rate. Kereš et al. (2005, 2009) have calculated volume-averaged accretion rates of cold gas at $z \simeq 0-7$ by performing cosmological hydrodynamics simulations. The simulations predict that the cold gas accretion rate shows an evolutional trend similar to the Madau-Lilly plot with a broad peak at $z \simeq 3$. As shown in Figure 4, we have indeed found that our $f_{\rm clumpy}^{\rm UV}$ evolution at $z \simeq 0-8$ is similar to such an evolutional trend of the cold gas accretion rate. This evolutional similarity suggests that a majority of clumps form through the VDI. The $f_{\text{clumpy}}^{\cup \vee}$ measurements beyond $z \simeq 3$ allow us to clearly identify the major clump formation mechanism over cosmic time.

The results of our clumpy structure analyses at $z \simeq 0-3$ are also consistent with the in-situ clump formation mechanism. The following arguments have been found in previous studies on clumpy galaxies at $z \lesssim 3$ (e.g., Guo et al. 2015). Our $z \simeq 0-3$ $f_{\rm clumpy}^{\rm UV}$ and n results would be explained by the evolution of unstable gas-rich galaxy disks. According to observations for gas fractions

and kinematics (e.g., Tacconi et al. 2010), $f_{\rm clumpy}^{\rm UV}$ is expected to decrease from $z\simeq 3$ to $z\simeq 0$ due to the disk stabilization towards low z. In Figure 3, we have indeed found that our $f_{\rm clumpy}^{\rm UV}$ shows such a decreasing trend at from $z\simeq 3$ to $z\simeq 0$. On the other hand, our $f_{\rm clumpy}^{\rm UV}$ correlates with the SF-related quantities of clumpy host galaxies (Section 6.3). These correlations could also be explained by the in-situ clump formation. The in-situ clump formation would enhance the global SF activity of clumpy host galaxies due to the vigorous star (clump) formation in galaxy disks. This enhancement of the SF activity would naturally result in a correlation between $f_{\rm clumpy}^{\rm UV}$ and the SF-related quantities.

All of our $z \simeq 0-3$ results also suggest the picture that a majority of clumps form in VDI. Combined with the discussion in Section 7.1.1, the major clump formation mechanism at $z \simeq 0-8$ is likely to be the VDI rather than the galaxy mergers.

7.2. Clump Migration

We discuss the evolution of clumps in galactic regions. We find that the clump color tends to be blue at a large $d_{\rm cl}/r_{\rm e}$, and tends to become red towards galactic centers for the clumpy galaxies with $\log M/M_{\odot} \gtrsim 11$ (Figure 12 and Section 6.4). This result suggests that clumps at outer galactic regions would be young if we assume that the blue $m_{\rm UV}-m_{\rm opt}$ color implies young stellar ages and/or low dust extinction. The color- $d_{\rm cl}/r_{\rm e}$ correlation would be explained by a scenario that such a young clump is evolved in the stellar population during the clump migration to the galactic centers (e.g., Dekel et al. 2009a; Krumholz & Dekel 2010; Förster Schreiber et al. 2011; Ceverino et al. 2012; Inoue & Saitoh 2012; Okamoto 2013; Mandelker et al. 2014). In contrast, we find that no strong color- $d_{\rm cl}/r_{\rm e}$ correlation is shown for the low- M_* and the intermediate- M_* clumpy galaxies with $\log M/M_{\odot} = 9 - 11$. The no correlation indicates that clumps may be destroyed by galaxy feedback effects before the clump migration in galaxies with $\log M/M_{\odot} \simeq 9-11.$

8. SUMMARY AND CONCLUSION

We present the redshift evolution of $f_{\rm clumpy}$ and investigate the properties of clumpy host galaxies using the HST samples of galaxies at $z\simeq 0-8$. Our HST samples consist of photo-z galaxies at z=0-6 from the 3D-HST+CANDELS catalogue and LBGs at $z\simeq 4-8$ identified in CANDELS, HUDF09/12, and HFF parallel fields. The large galaxy sample allows for the systematic search for clumpy galaxies over the wide-redshift range of $z\simeq 0-8$. We identify clumpy galaxies with off-center clumps in a self-consistent clump detection algorithm for the HST sample, and measure $f_{\rm clumpy}$ at $z\simeq 0-8$.

We summarize our major findings below.

1. We identify an evolutional trend of $f_{\rm clumpy}^{\rm UV}$ over $z\simeq 0-8$ for the first time: $f_{\rm clumpy}^{\rm UV}$ increases from $z\simeq 8$ to $z\simeq 1-3$ and decreases from $z\simeq 1$ to $z\simeq 0$. This $f_{\rm clumpy}^{\rm UV}$ trend is similar to the "Madau-Lilly" plot of the cosmic SFR density evolution. We test whether the $f_{\rm clumpy}^{\rm UV}$ trend is caused by difficulties of the clump identification at high z. We confirm

 $^{^9}$ The existence of galaxy disks at $z\gtrsim 3$ is also supported by numerical simulations (e.g., Romano-Díaz et al. 2011; Yajima et al. 2015) and studies on galaxy sizes (e.g. Paper I).

that the evolutional $f_{\text{clumpy}}^{\text{UV}}$ trend is real based on the tests

- 2. We examine the underlying morphology of our clumpy galaxies. We obtain typical radial SB profiles by stacking the rest-frame optical images of our clumpy galaxies at $z \simeq 0-2$. Our median stacking analysis enables us to examine underlying components of clumpy host galaxies, negligibly affected by flux contributions of individual clumps. The best-fit Sérsic indices to these radial SB profiles show a low value of $n \simeq 1$. These low n values indicate that clumpy galaxies tend to have disk-like structures.
- 3. We investigate relations between $f_{\rm clumpy}^{\rm UV}$ and physical quantities of host galaxies. We find that $f_{\rm clumpy}^{\rm UV}$ tends to increase with increasing the SF-related quantities (i.e., SFR, sSFR, $\Sigma_{\rm SFR}$) for the photo-z galaxies at $z\simeq 0-2$. We also identify trends that $f_{\rm clumpy}^{\rm UV}$ increases for $z\simeq 4-7$ LBGs with a bright $M_{\rm UV}$, a high $\Sigma_{\rm SFR}$, and a blue UV slope. These relations suggest that the clump formation would be intimately related to the entire SF activity of host galaxies.
- 4. We find a trend that the clump $m_{\rm UV}-m_{\rm opt}$ colors are red at a small galactocentric distance $d_{\rm cl}/r_{\rm e}$ for massive galaxies with $\log M_*/M_{\odot}=11-12$. The color- $d_{\rm cl}/r_{\rm e}$ correlations would be evidence that young clumps at galaxy disks migrate into the galactic centers. The clump color trends tend to be marginal for intermediate- M_* and $\log M_*/M_{\odot}=9-11$. The clumps may be destroyed by galaxy feedback effects before the clump migration for these galaxies with $\log M_*/M_{\odot}=9-11$.

In Figure 5, we find that $f_{\text{clumpy}}^{\text{UV}}$ does not show the evolutional trends similar to those of the galaxy major

and minor merger fractions, but the one of the cold gas accretion rate. All of these results are consistent with a picture that a majority of clumps form in the violent disk instability and migrate into the galactic centers.

The morphology of inner galactic regions remains unknown for compact sources with $r_{\rm e} \lesssim 0.22$ in the spatial resolution of PSF $\gtrsim 0.12$ in FWHM of HST. According to the evolution of galaxy size-luminosity relations, galaxies at $z \gtrsim 3$ tend to be as small as $r_{\rm e} \lesssim 1$ kpc, corresponding to $r_{\rm e} \lesssim 0.22$ (e.g. Paper I). The morphology of the inner regions for these compact galaxies will be revealed by future space missions and 30-meter class telescopes that resolve galaxy structures with a physical scale of $\gtrsim 0.05$ kpc at $z \simeq 7-15$ (Skidmore et al. 2015; Holwerda et al. 2015).

We would like to thank Yicheng Guo, Masao Hayashi, Masaru Kajisawa, Nobunari Kashikawa, Ryota Kawamata, Masakazu A. R. Kobayashi, Takahiro Morishita, Kentaro Motohara, Katsuhiro L. Murata, Kentaro Nagamine, Kouji Ohta, Takashi Okamoto, Masao Mori, Rhythm Shimakawa, Kazuhiro Shimasaku, Kenichi Tadaki, and Masayuki Umemura for useful discussion and comments. This work is based on observations taken by the 3D-HST Treasury Program (GO 12177 and 12328) and CANDELS Multi-Cycle Treasury Program with the NASA/ESA HST, which is operated by the Association of Universities for Research in Astronomy, Inc., under NASA contract NAS5-26555. Support for this work was provided by NASA through an award issued by JPL/Caltech. This work was supported by World Premier International Research Center Initiative (WPI Initiative), MEXT, Japan, KAKENHI (23244025), (21244013), and (15H02064) Grant-in-Aid for Scientific Research (A) through Japan Society for the Promotion of Science (JSPS), and an Advanced Leading Graduate Course for Photon Science grant.

Facilities: HST (ACS, WFC3).

D. A. 2007, ApJ, 658, 763

REFERENCES

Agertz, O., Romeo, A. B., & Grisdale, K. 2015, MNRAS, 449, 2156
Agertz, O., Teyssier, R., & Moore, B. 2009, MNRAS, 397, L64
Atek, H., et al. 2015, ApJ, 800, 18
Beckwith, S. V. W., et al. 2006, AJ, 132, 1729
Bertin, E., & Arnouts, S. 1996, A&AS, 117, 393
Birnboim, Y., & Dekel, A. 2003, MNRAS, 345, 349
Bluck, A. F. L., Conselice, C. J., Bouwens, R. J., Daddi, E.,
Dickinson, M., Papovich, C., & Yan, H. 2009, MNRAS, 394,
L51
Bournaud, F. 2015, ArXiv e-prints
Bournaud, F., Elmegreen, B. G., & Elmegreen, D. M. 2007, ApJ,
670, 237
Bournaud, F., et al. 2008, A&A, 486, 741
— 2014, ApJ, 780, 57
Bouwens, R. J., et al. 2011, ApJ, 737, 90
— 2014a, ApJ, 793, 115
— 2014b, ArXiv e-prints
Bundy, K., Fukugita, M., Ellis, R. S., Targett, T. A., Belli, S., &
Kodama, T. 2009, ApJ, 697, 1369
Burkert, A., et al. 2015, ArXiv e-prints
Cassata, P., et al. 2005, MNRAS, 357, 903
Ceverino, D., Dekel, A., & Bournaud, F. 2010, MNRAS, 404, 2151
Ceverino, D., Dekel, A., Mandelker, N., Bournaud, F., Burkert,
A., Genzel, R., & Primack, J. 2012, MNRAS, 420, 3490
Chabrier, G. 2003, PASP, 115, 763
Coe, D., Bradley, L., & Zitrin, A. 2014, ArXiv e-prints
Cole, S., et al. 2001, MNRAS, 326, 255

Conselice, C. J. 2003, ApJS, 147, 1
Conselice, C. J., & Arnold, J. 2009, MNRAS, 397, 208
Conselice, C. J., Bluck, A. F. L., Mortlock, A., Palamara, D., & Benson, A. J. 2014, MNRAS, 444, 1125
Cowie, L. L., Hu, E. M., & Songaila, A. 1995, AJ, 110, 1576
Curtis-Lake, E., et al. 2014, ArXiv e-prints
Dekel, A., & Birnboim, Y. 2006, MNRAS, 368, 2
Dekel, A., Sari, R., & Ceverino, D. 2009a, ApJ, 703, 785
Dekel, A., et al. 2009b, Nature, 457, 451
Di Matteo, P., Bournaud, F., Martig, M., Combes, F., Melchior, A.-L., & Semelin, B. 2008, A&A, 492, 31
Ellis, R. S., et al. 2013, ApJ, 763, L7
Elmegreen, B. G., Bournaud, F., & Elmegreen, D. M. 2008, ApJ, 688, 67
Elmegreen, B. G., & Elmegreen, D. M. 2005, ApJ, 627, 632
— 2006, ApJ, 650, 644
Elmegreen, B. G., Elmegreen, D. M., Fernandez, M. X., & Lemonias, J. J. 2009a, ApJ, 692, 12
Elmegreen, B. G., Elmegreen, D. M., Sánchez Almeida, J., Muñoz-Tuñón, C., Dewberry, J., Putko, J., Teich, Y., & Popinchalk, M. 2013, ApJ, 774, 86
Elmegreen, D. M., Elmegreen, B. G., & Ferguson, T. E. 2005, ApJ, 623, L71
Elmegreen, D. M., Elmegreen, B. G., & Hirst, A. C. 2004, ApJ, 604, L21
Elmegreen, D. M., Elmegreen, B. G., Marcus, M. T., Shahinyan, K., Yau, A., & Petersen, M. 2009b, ApJ, 701, 306
Elmegreen, D. M., Elmegreen, B. G., Ravindranath, S., & Coe,

Fakhouri, O., Ma, C.-P., & Boylan-Kolchin, M. 2010, MNRAS, 406, 2267
Forbes, J., Krumholz, M., & Burkert, A. 2012, ApJ, 754, 48
Förster Schreiber, N. M., et al. 2011, ApJ, 739, 45
Galametz, A., et al. 2013, ApJS, 206, 10
Garland, C. A., Pisano, D. J., Mac Low, M.-M., Kreckel, K., Rabidoux, K., & Guzmán, R. 2015, ApJ, 807, 134
Genel, S., Genzel, R., Bouché, N., Naab, T., & Sternberg, A. 2009, ApJ, 701, 2002
Genel, S., et al. 2008, ApJ, 688, 789
— 2012, ApJ, 745, 11
Genzel, R., et al. 2011, ApJ, 733, 101
— 2014, ApJ, 796, 7
Giavalisco, M., Livio, M., Bohlin, R. C., Macchetto, F. D., & Stecher, T. P. 1996, AJ, 112, 369
Glazebrook, K. 2013, pasa, 30, 56
Grogin, N. A., et al. 2011, ApJS, 197, 35
Guaita, L., et al. 2015, A&A, 576, A51
Guo, Y., Giavalisco, M., Ferguson, H. C., Cassata, P., & Koekemoer, A. M. 2012, ApJ, 757, 120
Guo, Y., et al. 2013, ApJS, 207, 24
— 2015, ApJ, 800, 39
Holwerda, B. W., Bouwens, R., Oesch, P., Smit, R., Illingworth, G., & Labbe, I. 2015, ApJ, 808, 6
Hopkins, P. F., Kereš, D., Murray, N., Quataert, E., & Hernquist, L. 2012, MNRAS, 427, 968
Hopkins, P. F., et al. 2010, ApJ, 724, 915
Hubble, E. P. 1926, ApJ, 64, 321
Huertas-Company, M., et al. 2015, ArXiv e-prints
Illingworth, G. D., et al. 2013, ApJS, 209, 6
Immeli, A., Samland, M., Gerhard, O., & Westera, P. 2004a, A&A, 413, 547
Immeli, A., Samland, M., Westera, P., & Gerhard, O. 2004b, Fakhouri, O., Ma, C.-P., & Boylan-Kolchin, M. 2010, MNRAS, 406, 2267Immeli, A., Samiand, M., Gernard, O., & Westera, P. 2004a, A&A, 413, 547
Immeli, A., Samland, M., Westera, P., & Gerhard, O. 2004b, ApJ, 611, 20
Inoue, S., Dekel, A., Mandelker, N., Ceverino, D., Bournaud, F., Inoue, S., Dekel, A., Mandelker, N., Ceverino, D., Bournaud, r., & Primack, J. 2015, ArXiv e-prints
Inoue, S., & Saitoh, T. R. 2012, MNRAS, 422, 1902
Ishigaki, M., Kawamata, R., Ouchi, M., Oguri, M., Shimasaku, K., & Ono, Y. 2014, ArXiv e-prints
Jiang, L., et al. 2013, ApJ, 773, 153
Jones, T. A., Swinbank, A. M., Ellis, R. S., Richard, J., & Stark, D. P. 2010, MNRAS, 404, 1247
Kawamata R. Ishigaki, M., Shimasaku, K., Oguri, M., & Ouchi, Kawamata, R., Ishigaki, M., Shimasaku, K., Oguri, M., & Ouchi, M. 2014, ArXiv e-prints
Kennicutt, Jr., R. C. 1998, ApJ, 498, 541
Kereš, D., Katz, N., Fardal, M., Davé, R., & Weinberg, D. H. 2009, MNRAS, 395, 160 Kereš, D., Katz, N., Weinberg, D. H., & Davé, R. 2005, MNRAS, 363, 2
Kereš, D., Vogelsberger, M., Sijacki, D., Springel, V., & Hernquist, L. 2012, MNRAS, 425, 2027
Koekemoer, A. M., et al. 2011, ApJS, 197, 36
Komatsu, E., et al. 2011, ApJS, 192, 18
Kron, R. G. 1980, ApJS, 43, 305
Krumholz, M. R., & Dekel, A. 2010, MNRAS, 406, 112
Kubo, M., Yamada, T., Ichikawa, T., Kajisawa, M., Matsuda, Y., Tanaka, I., & Umehata, H. 2015, ArXiv e-prints
Kubo, M., et al. 2013, ApJ, 778, 170
Law, D. R., Steidel, C. C., Shapley, A. E., Nagy, S. R., Reddy, N. A., & Erb, D. K. 2012a, ApJ, 759, 29
—. 2012b, ApJ, 745, 85
Le Fèvre, O., et al. 2000, MNRAS, 311, 565
Lilly, S. J., Le Fevre, O., Hammer, F., & Crampton, D. 1996, ApJ, 460, L1
Livermore, R. C., et al. 2012, MNRAS, 427, 688 ApJ, 460, L1
Livermore, R. C., et al. 2012, MNRAS, 427, 688
— 2015, MNRAS, 450, 1812
López-Sanjuan, C., et al. 2013, A&A, 553, A78
Lotz, J. M., Jonsson, P., Cox, T. J., Croton, D., Primack, J. R., Somerville, R. S., & Stewart, K. 2011, ApJ, 742, 103
Lotz, J. M., Madau, P., Giavalisco, M., Primack, J., & Ferguson, H. C. 2006, ApJ, 636, 592
Madau, P., & Dickinson, M. 2014, ARA&A, 52, 415

Madau, P., Ferguson, H. C., Dickinson, M. E., Giavalisco, M., Steidel, C. C., & Fruchter, A. 1996, MNRAS, 283, 1388
Man, A. W. S., Toft, S., Zirm, A. W., Wuyts, S., & van der Wel, A. 2012, ApJ, 744, 85
Man, A. W. S., Zirm, A. W., & Toft, S. 2014, ArXiv e-prints
Mandelker, N., Dekel, A., Ceverino, D., Tweed, D., Moody, C. E., & Primack, J. 2014, MNRAS, 443, 3675
Menéndez-Delmestre, K., Blain, A. W., Swinbank, M., Smail, I., Ivison, R. J., Chapman, S. C., & Gonçalves, T. S. 2013, ApJ, 767, 151 767, 151Moody, C. E., Guo, Y., Mandelker, N., Ceverino, D., Mozena, M., Koo, D. C., Dekel, A., & Primack, J. 2014, MNRAS, 444, 1389 Morishita, T., Ichikawa, T., Noguchi, M., Akiyama, M., Patel, S. G., Kajisawa, M., & Obata, T. 2015, ArXiv e-prints Murata, K. L., et al. 2014, ApJ, 786, 15 Nelson, D., Vogelsberger, M., Genel, S., Sijacki, D., Kereš, D., Springel, V., & Hernquist, L. 2013, MNRAS, 429, 3353 Springel, V., & Hernquist, L. 2013, MINRAS, 429, 3353
Nelson, E. J., et al. 2015, ArXiv e-prints
Newman, S. F., et al. 2012, ApJ, 752, 111
Noguchi, M. 1998, Nature, 392, 253
Oesch, P. A., Bouwens, R. J., Illingworth, G. D., Franx, M.,
Ammons, S. M., van Dokkum, P. G., Trenti, M., & Labbe, I.
2014, ArXiv e-prints
Oesch, P. A., et al. 2010, ApJ, 709, L21
Okamoto, T. 2013, MNRAS, 428, 718
Oke, J. B. & Gunn, J. E. 1983, ApJ, 266, 713 Oke, J. B., & Gunn, J. E. 1983, ApJ, 266, 713 Oke, J. B., & Gunn, J. E. 1983, ApJ, 266, 713
Overzier, R. A., Heckman, T. M., Schiminovich, D., Basu-Zych, A., Gonçalves, T., Martin, D. C., & Rich, R. M. 2010, ApJ, 710, 979
Patel, S. G., et al. 2013, ApJ, 766, 15
Peng, C. Y., Ho, L. C., Impey, C. D., & Rix, H.-W. 2002, AJ, 124, 266 124, 200 —. 2010, AJ, 139, 2097 Puech, M. 2010, MNRAS, 406, 535 Ravindranath, S., et al. 2006, ApJ, 652, 963 Rodriguez-Gomez, V., et al. 2015, MNRAS, 449, 49 Romano-Díaz, E., Choi, J.-H., Shlosman, I., & Trenti, M. 2011, Romano-Diaz, E., Choi, J.-H., Shlosman, I., & Trenti, M. 201 ApJ, 738, L19
Salpeter, E. E. 1955, ApJ, 121, 161
Sérsic, J. L. 1963, Boletin de la Asociacion Argentina de Astronomia La Plata Argentina, 6, 41

— 1968, Atlas de galaxias australes (Sérsic, J. L.)
Shapiro, K. L., et al. 2008, ApJ, 682, 231
Shibuya, T., Ouchi, M., & Harikane, Y. 2015, ArXiv e-prints
Skelton, R. E., et al. 2014, ArXiv e-prints
Skidmore, W., et al. 2015, ArXiv e-prints
Sobral D. et al. 2013, ApJ, 779, 139 Skeiton, R. E., et al. 2015, ArXiv e-prints
Skidmore, W., et al. 2015, ArXiv e-prints
Sobral, D., et al. 2013, ApJ, 779, 139
Steidel, C. C., Adelberger, K. L., Giavalisco, M., Dickinson, M.,
& Pettini, M. 1999, ApJ, 519, 1
Swinbank, A. M., et al. 2009, MNRAS, 400, 1121
Tacchella, S., et al. 2015, ApJ, 802, 101
Tacconi, L. J., et al. 2010, Nature, 463, 781
Tadaki, K.-i., Kodama, T., Tanaka, I., Hayashi, M., Koyama, Y.,
& Shimakawa, R. 2014, ApJ, 780, 77
Taniguchi, Y., & Shioya, Y. 2001, ApJ, 547, 146
Toomre, A. 1964, ApJ, 139, 1217
van den Bergh, S., Abraham, R. G., Ellis, R. S., Tanvir, N. R.,
Santiago, B. X., & Glazebrook, K. G. 1996, AJ, 112, 359
van Dokkum, P. G., et al. 2010, ApJ, 709, 1018
Williams, J. P., de Geus, E. J., & Blitz, L. 1994, ApJ, 428, 693
Williams, R. J., Quadri, R. F., & Franx, M. 2011, ApJ, 738, L25
Wisnioski, E., Glazebrook, K., Blake, C., Poole, G. B., Green,
A. W., Wyder, T., & Martin, C. 2012, MNRAS, 422, 3339
Wisnioski, E., Glazebrook, K., Blake, C., & Swinbank, A. M.
2013, MNRAS, 436, 266
Wisnioski, E., et al. 2011, MNRAS, 417, 2601
Wuyts, S., et al. 2012, ApJ, 753, 114 Wuyts, S., et al. 2012, ApJ, 753, 114 Yajima, H., Shlosman, I., Romano-Díaz, E., & Nagamine, K. 2015, MNRAS, 451, 418